IN-24
137548
p-50

NASA Contractor Report 189096–Part II

Inelastic Deformation of Metal Matrix Composites: Plasticity and Damage Mechanisms – Part II

B.S. Majumdar and G.M. Newaz
Battelle
Columbus, Ohio

December 1992

(NASA-CR-189096-Pt-2) INELASTIC DEFORMATION OF METAL MATRIX COMPOSITES: PLASTICITY AND DAMAGE MECHANISMS, PART 2 Final Report (Battelle Columbus Labs.) 50 p

N93-15401

Unclas

G3/24 0137548

NASA

INELASTIC DEFORMATION OF METAL MATRIX COMPOSITES: PART II, PLASTICITY AND DAMAGE AT HIGH TEMPERATURES

PART II (SECOND HALF) OF FINAL REPORT

TO

NASA LEWIS RESEARCH CENTER
HITEMP OFFICE

CONTRACT NO. NAS3 - 26053

Bhaskar S. Majumdar and Golam M. Newaz

BATTELLE
Metals & Ceramics Department
505 King Avenue
Columbus, Ohio 43201

June 2, 1992

TABLE OF CONTENTS

Page

1. INTRODUCTION 1
2. EXPERIMENTS 2
3. RESULTS 4
    3.1 Mechanical Test Results 4
        3.1.1 $[0]_8$ MMC 4
            3.1.1.1 Monotonic Tension Test Results 4
            3.1.1.2 Creep Test Results 5
        3.1.2 $[90]_8$ MMC 8
            3.1.2.1 Monotonic Tension Test Results 8
            3.1.2.2 Creep Test Results 9
        3.1.3 $[\pm45]_{2s}$ MMC 10
            3.1.3.1 Tension Test Results 10
        3.1.4 $[0/90]_{2s}$ MMC 11
            3.1.4.1 Tension Test Results 11
    3.2 Microstructure 12
        3.2.1 $[0]_8$ MMC 12
        3.2.2 $[90]_8$ MMC 13
        3.2.3 $[\pm45]_{2s}$ MMC 13
        3.2.4 $[0/90]_{2s}$ MMC 14
4. COMPARISONS OF THEORY WITH EXPERIMENTS 15
5. DISCUSSION 18
6. CONCLUSIONS 20
7. ACKNOWLEDGMENTS 21
8. REFERENCES 22

9. FIGURES

INELASTIC DEFORMATION OF METAL MATRIX COMPOSITES: PART II, PLASTICITY AND DAMAGE AT HIGH TEMPERATURES

B. S. Majumdar and G. M. Newaz
Battelle
505 King Avenue, Columbus, Ohio 43201

ABSTRACT

This report constitutes the second half of Battelle's Final Report to the HITEMP Office, NASA Lewis Research Center, under Contract No. NAS3-26053. The program monitor at NASA Lewis was Dr. J.R. Ellis, and the program manager at Battelle was Dr. B.S. Majumdar. Whereas in Part I, the room temperature inelastic deformation mechanisms for a Ti 15-3/SCS6 (SiC) system were described, in this report (Part II) the results of high temperature experiments are discussed.

The inelastic deformation mechanisms for the Ti 15-3/SCS6 (SiC) system were investigated at 538 C (1000 F) using a combination of mechanical measurements and detailed microstructural examinations. The objectives were to evaluate the contributions of plasticity and damage to the overall MMC response, and to compare the room temperature and elevated temperature deformation behaviors. Four different laminates were investigated: $[0]_8$, $[90]_8$, $[\pm 45]_{2s}$, and $[0/90]_{2s}$ systems, with primary emphasis on the unidirectional $[0]_8$ and $[90]_8$ systems. Strains were monitored in the loading direction and also transverse to the loading direction, using a set of three extensometers. The elevated temperature responses were similar to those at room temperature, involving a two-stage elastic-plastic type of response for the $[0]_8$ system, and a characteristic three-stage deformation response for the $[90]_8$ and $[\pm 45]_8$ systems. Thus, a good understanding of the deformation behavior at room temperature, where experiments are relatively simple, can provide very valuable insight into mechanisms that may operate at elevated temperatures. The primary effects of elevated temperature included: (i) reductions in the "yield" and failure strengths, (ii) plasticity occurred through diffused slip rather than planar concentrated slip (which occurred at room temperature), and, (iii) there was time-dependent deformation, with significant creep occurring at low stresses (<30 MPa) for the $[90]_8$ MMC. The density of reaction-zone cracks were also found to be less at 538 C compared with room temperature. The inelastic deformation mechanism for the $[0]_8$ MMC was dominated by plasticity at both temperatures. For the $[90]_8$ and $[\pm 45]_{2s}$ MMCs, a combination of damage and plasticity contributed to the inelastic deformation at both temperatures. The experimental results were compared with the predictions of

three constitutive models: METCAN, AGLPLY, and a recent unit-cell finite element method (FEM) model developed at Battelle. The comparisons showed that both the METCAN and AGLPLY codes needed some refinements for adequately predicting the stress-strain response of laminates, particularly those having fibers perpendicular to the loading direction. The unit-cell model, although more complex, appeared to provide best correlation with the experimental data for the unidirectional MMCs.

1. INTRODUCTION

Structural designs with metal matrix composites (MMCs) require: (1) a suitable constitutive model, such that stresses and strains can be computed *locally* (such as those at the fiber/matrix/interface level) in a structure, and (2) the establishment of *failure criteria* which govern functional loss under different loading conditions. For time-dependent loadings, there is also the issue of time or cycle-dependent creep and damage, which require that the computation of local stresses and strains incorporate the progression (or growth law) of permanent deformation/damage in the composite. All these ingredients require detailed knowledge of the material's *elastic* and *inelastic* (i.e., permanent) deformation mechanisms (see Figure 1). Understanding the inelastic processes also is important from a materials development perspective, because the information can guide in suitably modifying MMC architecture and processing history for obtaining higher levels of critical stresses and strains, by favorably shifting the onset of non-linearity in the stress-strain curve.

The need to understand the deformation mechanisms formed the rationale for the work described here. A Ti 15-3/SCS-6 composite was chosen as the model material, and experiments were selected for identifying the important deformation processes. In Part I of this work [1], and related papers [2-5], we have illustrated some of the important mechanisms that were observed at room temperature, and clarified the sequences of plasticity and damage. By *plasticity* we imply processes involving dislocation nucleation and motion, and would include changes in dislocation density, morphology, or twinning. By *damage* we imply formation of new and free surfaces except slip steps that are formed on a specimen surface by plastic deformation; damage would include cracking of fibers, matrix, fiber-matrix reaction zone, or debonding at the fiber-matrix interface. It was shown conclusively [1-5], using a combination of mechanical experiments and detailed optical microscopy and transmission electron microscopy (TEM), that inelastic deformation of the 0° MMC at room temperature was dominated by plasticity. However, reaction-zone cracks played the important role of nucleating slip bands in the micro-yield regime of deformation, and was expected to play an important role in fatigue. For the 90° MMC, damage became the dominant deformation mechanism at low strains, and at larger strains, plasticity appeared to dominate. Comparisons also were made with theoretical predictions, and it was shown that although a model might appear to predict the longitudinal stress-strain response of a MMC reasonably well, it might fall far short in predicting the transverse strains; i.e., rigorous validation was necessary before a model was accepted as being representative of actual MMC behavior. The results of other investigations on Ti-based MMCs which are relevant to the research described here and in Part I, are available in references [6-8].

The work described here represents a continuation of the room-temperature experiments to elevated-temperature tension-loading situations. The emphasis once again was to clarify important issues regarding plasticity and damage, and to evaluate critical mechanisms that operated at high temperatures. As will be shown later, the primary mechanisms appeared not to be significantly influenced by temperature, except for their degree of influence, and the fact that the magnitude of deformation became time-dependent at elevated temperatures. Thus, the present results appear to suggest that detailed investigation of room temperature deformation (where experiments are significantly less complex than at elevated temperatures) can provide important insights into overall deformation behavior of MMCs. However, only monotonic tension loading and limited creep experiments were performed, and it is likely that new mechanisms might operate under fatigue and thermal-mechanical fatigue (TMF) situations.

2. EXPERIMENTS

As indicated in Part I [1], the approach that was taken in this work was to confirm the deformation behavior using a combination of mechanical experiments and detailed microstructural examinations. For example, if plasticity was dominant during the inelastic regime of deformation, then the specimen unloading compliance would be anticipated to remain identical to the initial loading compliance, and also a significant strain offset would be observed at zero load. Conversely, under damage, the specimen unloading compliance would be larger than the initial compliance, and no strain offset would be present at zero load.

Another good technique for clarifying issues of plasticity and damage using mechanical measurements is to monitor the material's Poisson's ratio. Thus, for a $[0]_8$ lamina MMC (a unidirectional MMC loaded in the fiber direction), the instantaneous Poisson's ratio would be anticipated to increase if plasticity was dominant, and would decrease if damage was dominant. An advantage of the Poisson's ratio technique is that it does not require specimen unloading, and also we found the measurements to be extremely useful for determining the effectiveness of various constitutive models [1-4].

Finally, microstructural evaluation can provide direct evidence of plasticity and damage. The former will be manifested as changed dislocation configurations and slip bands. The latter will be manifested as cracks and fiber-matrix separations.

The materials tested were 8-ply Ti 15-3/SCS-6 composites, approximately 1.99 mm thick, fabricated by Textron using a foil-fiber-foil consolidation technique; the fiber volume fraction was approximately 0.34. The SCS-6 (SiC) fiber diameter is approximately 140 µm, and it contains alternating outer layers of C and non-stoichiometric SiC, which protect the fiber from cracking during handling. The Ti 15-3 (Ti-15V-3Cr-3Al-3Sn, all in weight percent) alloy is a metastable body centered cubic (bcc) β Ti-alloy, the bcc phase being stabilized by vanadium. Metastability occurs because hexagonal ω and α phases precipitate in the β bcc matrix when it is held at intermediate temperatures.

Uniaxial tensile test specimens, of width 8.9 mm in gage region and 12.7 mm in grip region, and possessing a gage length of 25.4 mm, were machined from the unidirectional panel using an electric-discharge machining (EDM) technique; specimen thickness was approximately 2 mm. The specimens were mechanically polished after EDM cutting to remove any damage associated with machining. The following layups were investigated: $[0]_8$, $[90]_8$, $[\pm45]_{2s}$, $[0/90]_{2s}$ systems, and a 4-ply Ti 15-3 matrix material. The $[0]_8$, $[90]_8$, and matrix specimens were tested in the as-fabricated condition, involving a cool-down from the HIP-ing temperature of approximately 815 C; no heat-treatment was performed prior to the testing. The $[\pm45]_{2s}$ and $[0/90]_{2s}$ specimens received a 700 C/24 hours heat treatment prior to being tested. However, as indicated in references [1-5], the stress-strain behavior of the $[0]_8$ and $[90]_8$ composites were not significantly different at room temperature for the material with and without the 700 C heat treatment.

Specimens were gripped using friction grips, and loaded on a servohydraulic testing machine. Induction coils were used to heat the specimens, and all testing was performed in air. Most of the elevated temperature experiments were performed at 538 C (1000 F), and a few were performed at 649 C (1200 F); elevated temperature tension tests were performed at a strain rate of 10^{-4}/sec, unless stated otherwise in the plots provided later. Tension tests lasted a few minutes at temperature, and creep tests were run for a maximum period of 4 hours at 538 C. The emphasis in creep tests was more to understand the dominant deformation mechanisms than to evaluate the stress-rupture behavior. Although oxidation is an issue for the temperatures investigated, tension-test specimens did not reveal significant oxide scales or alpha-case; thus, we believe that the stress-strain responses observed were not greatly influenced by the short period of exposure at the test temperature. In addition to longitudinal strains (along specimen axis), the width and thickness strains were monitored using extensometers with ceramic arms; strain gages were also used for room temperature experiments and provided data in agreement with those from the extensometers. Figure 2 shows the experimental setup for the elevated temperature experiments.

Following mechanical testing, specimens were sectioned slowly using a diamond wafering blade; significant debonding and fiber cracking can occur during machining if adequate care is not taken during sectioning. Sections were made perpendicular to the specimen axis (transverse cross section), and the center of the specimen width, but parallel to the specimen axis (edge cross section). This latter cross-sectioning technique was performed to reveal the bulk behavior, rather than effects associated with edges of mechanical test specimens. Specimens were metallographically polished, with the polished surfaces corresponding either to the face of the test specimen, or the edge and transverse cross sections. Faces were polished at the surface as well as up to the first set of fibers. Repeated polishing was performed on a few tested and untested samples to confirm that cracking, debonding, or slip bands were due to deformation alone, and not associated with the polishing procedure. Specimens were etched using Kroll's reagent, which was found to be effective in revealing slip bands. Specimens were examined optically and using a scanning electron microscope (SEM) after unloading from various values of strains. Also, in a number of tests the specimen deformation was monitored using the replication technique, after the specimen was cooled. These evaluations helped to clarify the sequence in which inelastic deformation processes occurred.

3. RESULTS

3.1 Mechanical Test Results

3.1.1 $[0]_8$ MMC

3.1.1.1 Monotonic Tension Test Results

The stress versus longitudinal strain data for a few of the tested $[0]_8$ specimens are shown in Figure 3a. The stress-strain behavior at 538 C was similar to that at room temperature (RT), with the unloading line being parallel to the loading line, and with significant strain offsets occurring at zero load. Together these suggest that inelastic deformation at 538 C was likely dominated by plasticity, similar to the case of RT deformation.

The elevated temperature deformation response differed from the RT response primarily in terms of the stresses and strains at which inelastic deformation initiated and fracture occurred. Whereas inelastic deformation at RT initiated at a "yield" strain of approximately 0.55%, it was approximately 0.35% at 538 C. Changes in the residual stress in the matrix cannot account for this temperature effect, since elevated temperatures would reduce, rather than increase, the residual *tensile* axial stress in the matrix. Rather, the lowering of the critical strain likely reflects the lowering of the flow stress of the matrix, which was approximately 800 MPa at RT , and which was only 400 MPa at 538 C (see Figure 8). The lowering of the *strain to failure* likely reflects the fact that fibers have less residual compression at 538 C compared with RT, so that the mechanical strain required to fracture the fibers would be less at 538 C compared with RT. These arguments are qualitative, and accurate predictions of the stress-strain response and the failure stress would require adequate incorporation of the inelastic deformation sequence into a constitutive model. Comparisons of mechanical data with theoretical predictions will be provided later.

Figure 3b is a plot of the width strain (ε_W) versus the longitudinal strain (ε_L) at 538 C. The figure contains data from the monotonic tension test and creep test (at 800 MPa); the stress-strain behavior for these specimens were plotted in Figure 3a. The main point to note here is that in the inelastic regime of deformation there was an increase in the slope of the curves. The instantaneous value of the width Poisson's ratio ($d\varepsilon_W/d\varepsilon_L$) increased from approximately 0.34 to values between 0.45 and 0.6, in going from the elastic to the inelastic regime of deformation. Such increases again reflect that the primary deformation mechanism at 538 C was likely plasticity rather than damage, at least up to strains very close to the failure strain of the composite.

Figure 3c is a plot of the thickness strain versus the longitudinal strain for a specimen tested in monotonic tension at 538 C. This plot does not indicate any significant change in the thickness Poisson's ratio, which remained at approximately 0.28 throughout the experiment. The fact that the Poisson's ratio does *not decrease* again suggests that the deformation mechanism was not damage.

3.1.1.2 Creep Test Results

Figure 4a shows the stress-strain response for a creep test at 800 MPa at 538 C. The stress level was chosen such that the initial strain upon loading (i.e., 0.5 percent) would be slightly above the "yield" strain of approximately 0.35 percent, corresponding to the onset of inelastic deformation in a simple tension test at 538 C at a strain rate of 10^{-4}/sec. The specimen was unloaded after approximately 210 minutes. Once again it may be observed that the unloading line was parallel to the loading line, indicating that inelasticity was likely by time-dependent plasticity. The dominance of matrix creep also is illustrated in Figure 3b, which shows that the Poisson's ratio increased in going from the elastic into the inelastic regime of deformation. It is notable that the MMC accumulated a strain of approximately 0.2 percent within the relatively short period of creep exposure.

An additional interesting point with respect to the effect of creep deformation is the manner in which it may affect the residual strength at 538 C. If it is assumed that fast fracture is controlled by attainment of a critical strain (failure strain of fibers), then the extrapolation indicated by BC in Figure 4a suggests that the loss in strength (a traditional mechanistic approach for defining damage) due to creep would be AC (approximately 150 MPa). Although such experiments were not performed to validate the hypothesis, we suggest that such residual strength experiments following creep be performed, to evaluate how time-dependent *shake-down* of a structure affects its load bearing capability. The parameters in such experimentation would be the stress levels, and the periods of creep exposure.

Figure 4b illustrates the strain-time behavior for the above creep sample. In this figure, the solid line AB represents the initial loading period, and the solid line BC represents the period of creep exposure at 800 MPa. The strain-time data for the region BC in Figure 4b was differentiated using a seven-point least-squares best-fit procedure, and the strain-rate versus time data are illustrated in Figure 5a. In this plot, the dots represent data points, and the straight line is a best fit straight line with a time exponent of -n/(n-1), where n (=4.1) represents the matrix material's power-law creep stress exponent at 566 C [9]; i.e., the only parameter that was adjusted during the best-fit procedure was the coefficient (calculated as 0.000775). Figure 5a shows that the creep-rate for the MMC decreased rapidly as a power-law function of time. The dashed line in Figure 4b represents the integral of $(-0.000775/t^{n/n-1})$, and shows how well the power law dependence of strain-rate on time can represent actual strain-versus-time data.

We would like to note here that the n/(n-1) dependence of strain-rate on time is based on a simplistic one-dimensional model of an elastic fiber embedded in a power-law creeping matrix material. The model is similar to that in reference [10], but avoids the complications of including a boundary layer surrounding the fiber with its own power-law characteristics. The unique power-law dependence of strain-rate on time was not brought out in reference [10], but our current results indicate that this relationship may be characteristic of Ti-alloy based MMCs at elevated temperatures. Additional tests at other temperatures and applied stress levels are however necessary to check the adequacy of the representation, which may take on a phenomenological character if the power-law type time dependence of strain-rate was retained, but if the exponent was something other than n/(n-1). For example, the assumption that the matrix is creeping in the secondary stage with a power-law creep characteristic may not represent actual matrix behavior (particularly at a lower temperature), where the matrix stress is continually decreasing with time; thus, arguments in favor of a strain-rate versus $t^{n/(n-1)}$ relationship could become invalid under those circumstances.

A final point we would like to make here is with respect to the best-fit constant 0.000775. This value was well above any estimate based on a simple one-dimensional stress-transfer mechanism, indicating that the creep rates were higher than anticipated. In order to provide a quantitative idea of the creep acceleration involved, we have back-calculated the stress in the matrix from the total accumulated strain, assuming a one-dimensional model and elastic fibers; no assumption was necessary regarding how the matrix was creeping. The measured strain-rate was then plotted versus the stress in the matrix, so that comparisons could be made with data for the un-reinforced matrix. The dots in Figure 5b represent actual data, and the wavy line is a smooth curve through the data points. The square symbols and the best-fit straight line through them represent the secondary creep data for the un-reinforced matrix at 566 C [9]. The important points to note in Figure 5b are : (i) at high stresses, just after loading of the MMC, the matrix in the MMC creeps at rates comparable to that in the un-reinforced material, and (ii) at lower stresses (below 80 MPa), the creep rate of the matrix can be orders of magnitude higher in the MMC compared with that in the un-reinforced material. In particular, it may be observed that the matrix was still creeping at reasonable rates even though the stress had dropped to below 20 MPa, a very low number for any significant creep of the un-reinforced matrix. It is difficult to explain the high creep rates, particularly since the microstructure showed no fiber or matrix cracks after the unloaded creep sample was metallographically polished; also, the unloading line was parallel to the loading line, indicating the absence of damage. Additional experiments are needed to adequately characterize the MMC creep behavior, and establish any anomalous creep deformation of the matrix at low stresses in the presence of fibers. The experiments must be accompanied with appropriate modeling, which in turn must incorporate additional creep characteristics of the un-reinforced matrix, to account for the continuous manner in which load shedding occurs for the matrix material in a $[0]_8$ MMC.

3.1.2 $[90]_8$ MMC

3.1.2.1 Monotonic Tension Test Results

Figure 6a illustrates the stress-strain behavior for the $[90]_8$ MMC at three temperatures: RT, 538 C, 649 C. As already indicated in [1-5], this system had a three-stage deformation characteristic at RT: Stage I, where deformation was elastic, with an elastic modulus of approximately 111 GPa; Stage II, where the stress-strain curve had a lower slope than in Stage I; and Stage III, where the stress was almost constant with increasing strain. Figure 6a illustrates that the same three-stage deformation characteristic was retained at 538 C, although the stress/strain level for each stage was reduced considerably compared with RT. At 649 C, the stress at the onset of Stage II became so low that Stage I disappeared, and only Stages II and III were observed; note that 649 C is too high a temperature for any useful MMC application of the Ti 15-3 matrix material.

The loading-unloading lines in Figure 6a show significant compliance increases during Stage II, indicating that damage likely was dominant during that stage. In references [2,3,8], it was shown that this effect at RT was due to fiber-matrix debonding, and our metallographic investigations (to be described in a later section) indicate that the same mechanism was likely responsible for the compliance increase observed at 538 C (see Figure 6a). The small strain offset at zero load in Figure 6a is indicative of plasticity, and references [2,3] provided conclusive slip-band evidence that indeed limited plasticity was operating during Stage II at RT. Figure 6b is a plot of the width strain versus the longitudinal strain for the same specimen. The data points are indicated by dots, and the solid line is a least-squares best-fit polynomial representation of the loading data points. Figure 6b shows that the rate of increase of the width strain decreased with increased longitudinal strain, particularly for strains above 0.1 percent. The instantaneous Poisson's ratio was initially approximately 0.18, and it decreased to approximately 0.12 at a longitudinal strain of 0.22 percent. Such decreases suggest that damage mechanisms were operative in Stage II, in agreement with the compliance data at 538 C. It is interesting to note that whereas the Poisson's ratio decreased to approximately 0.007 immediately after the onset of Stage II at RT, it decreased to a range between 0.14 and 0.17 at 538 C. It is not clear whether such differences are due to the different residual stresses at the two temperatures. From a materials perspective, one possibility is that the bond strength between the fiber and the reaction-zone could increase with temperature (plasticity becoming easier at elevated temperatures), and this may have made debonding slightly more difficult at 538 C compared with RT. Additional evidence in support of a higher bond strength is provided later, where it is shown that computational models require the existence of a finite bond strength to explain the existence of a Stage I at 538 C; at RT the existence of a zero bond strength was sufficient to explain all mechanical test results.

Figure 7 shows the effect of strain-rate on the Stage I-Stage II response. The characteristic three-stage deformation response was retained at the higher rate. The primary effects of a higher strain-rate were the elevation of the stress/strain levels, due likely to a positive dependence of the matrix material's flow stress on the strain-rate. In particular, a stress increase of 50 MPa in going from B to B' is noteworthy. The Stage I-Stage II transition point, such as B, is associated with debonding between the fiber and the reaction-zone [2,3,8]. Since strain-rate is not known to influence elastic properties, at least for the rates that are under discussion here, the stress difference between B and B' suggests that plasticity must be involved at the transition point, implying in turn that localized plasticity may be playing an important role during fiber-matrix debonding. Such a conclusion is once again in agreement with microstructural observations [2,3], where slip bands were observed to nucleate at the top and bottom of fibers even before fiber-matrix debonding occurred.

The stress-strain behaviors of the 90° MMC and matrix material are summarized in Figure 8. In agreement with other studies on fiber-reinforced MMCs, this plot shows that the $[90]_8$ MMC always has inferior properties compared with the matrix material.

3.1.2.2 Creep Test Results

The strain-versus-time and stress-strain behavior for three $[90]_8$ MMC samples, creep tested at 538 C, are shown in Figures 9a and 9b, respectively. The applied stress levels were chosen such that they were at the Stage I-Stage II transition, or in the Stage I regime of deformation (see Figure 9b). The rationale for the lower stresses was to evaluate whether time-dependent relaxation of residual stresses could induce inelastic deformation at stresses below the Stage I-Stage II transition. Figures 9a and 9b indicate that indeed creep deformation can occur at stresses as low 28 MPa, and that indeed the transition point is highly time-dependent. Thus, from a design perspective, it may be worthwhile assuming that Stage II deformation starts at zero stress, at least at temperatures where creep deformation of the matrix can be significant.

Unlike the case of the $[0]_8$ MMC, where steady-state strain-rates were not achieved, Figure 9a shows that constant strain-rates were realized fairly quickly in the $[90]_8$ specimens. Additional longer time tests at other stresses and temperatures are needed to fully characterize the creep behavior of the $[90]_8$ MMC.

Figure 9c is a plot of the width strain versus the longitudinal strain for the creep specimen tested at 69 MPa. The initial instantaneous Poisson's ratio was approximately 0.20, a value slightly higher than in Figure 6c. The Poisson's ratio then decreased to 0.12, and finally fell to a value of approximately 0.056. It is likely that fiber-matrix debonding contributed significantly to the drop in Poisson's ratio, although at higher strains plasticity also contributed to greater debonding. Additional implications of the Poisson's ratio results can only be obtained from modeling studies, and verifying whether current understanding of creep behavior of the MMC can account for observed values of Poisson's ratios. In this regard, our past studies have shown that Poisson's ratio data can be very useful for comparing the effectiveness of different constitutive models.

3.1.3 $[\pm 45]_{2s}$ MMC

3.1.3.1 Tension Test Results

Figure 10a shows comparisons of the stress-strain response of the $[\pm 45]_{2s}$ MMC at RT and 538 C. At RT, there was once again a three-stage stress-strain response, with significant compliance increases occurring during Stage II. In reference [3], the RT compliance increase was explained in terms of fiber-matrix debonding, and it is likely that the same mechanism operates at 538 C, similar to the case of the $[90]_8$ MMC. The Stage I-Stage II transition occurred at stresses of approximately 200 MPa and 100 MPa at RT and 538 C, respectively. It is notable that these values were almost identical for the case of the $[90]_8$ MMC.

Figure 10b illustrates the width strain versus longitudinal strain behavior for the $[\pm 45]_{2s}$ MMC. The Poisson's ratio was approximately 0.4 at strains less than 0.2 percent, then it increased to approximately 0.51. These values do appear to be quite high compared with elastic values around 0.30-0.35. At high strains, quite opposite behaviors were observed at RT and 538 C. At RT, the Poisson's ratio increased even further, whereas at 538 C it decreased to approximately 0.26. It is difficult to comment on these values pending adequate modeling of the $[\pm 45]_{2s}$ MMC.

3.1.4 $[0/90]_{2s}$ MMC

3.1.4.1 Tension Test Results

The stress-strain behaviors of the $[0/90]_{2s}$ MMC at RT and 538 C are compared in Figure 11a. The points A and B in the figure signify the start of different regimes of deformation with different slopes, and the X's mark the failure of specimens. The slope of the unloading line (from a strain of approximately 0.6 percent) was less than the slope of the initial loading line, indicating the occurrence of damage beyond point A. We believe this was due to debonding type of damage for the 90-degree plies. However, it is interesting to note that the onset of inelastic deformation at RT occurred at a strain of approximately 0.1 percent, which was lower than the critical strain of approximately 0.2 percent for the $[90]_8$ system (see Figure 6a). We believe that this effect was likely due to less compressive residual stress in the 90-degree plies of the $[0/90]_{2s}$ system compared with the unidirectional $[90]_8$ MMC.

At RT, the elastic modulus was approximately 141 GPa, and it decreased to approximately 111 GPa at 538 C. The failure strain also decreased from approximately 1 percent at RT to approximately 0.7 percent at 538 C. The decreases in the strain to failure were similar to the case of the $[0]_8$ specimens, where also decreases in strain to failure were of 0.3 to 0.4 percent were observed. The decrease in the failure strain with increasing temperatures are likely associated with lower residual axial compressive stresses in the 0-degree fibers at higher temperatures.

Figures 11b and 11c illustrate the transverse strain response and the instantaneous Poisson's ratio, respectively, for the $[0/90]_{2s}$ MMC. The results of Lerch et al.were obtained from reference [7], which contains a nice combined analyitical/experimental treatment of the $[0/90]_{2s}$ system. The initial Poisson's ratio was approximately 0.21, and after the onset of inelastic deformation it showed a plateau type of behavior, where the Poisson's ratio (ν) ranged between 0.14 and 0.17. Beyond a strain of approximately 0.6 percent, coincident with the second knee in the stress-strain curves, the Poisson's ratio fell even further, and attained a value of approximately 0.02 when fracture occurred. These low values are indicative of significant damage in the 90-degree plies.

3.2 Microstructure

3.2.1 $[0]_8$ MMC

Figures 12a and 12b show the microstructures of the $[0]_8$ MMC, tension tested to failure at RT and 538 C, respectively. The volume fraction of fibers appear different in the two micrographs because in Figure 12a the specimen had been polished down to the fiber core, whereas in Figure 12b the specimen was not polished down to that level. At both temperatures, there was no evidence of matrix or fiber cracking, and inelastic deformation appeared to be dominated by plasticity of the Ti 15-3 matrix. However, there was one primary difference in the plasticity mechanism at the two temperatures. At RT, sharp slip bands (sb) were observed, which are believed to be due to a very fine coherent ω-phase being present in the microstructure [1-3]. On the other hand, Figure 12b shows that there were only diffused slip bands at 538 C, consistent with the expectation that easier cross slip at elevated temperatures would contribute to diffused slip rather than planar slip.

In reference [2,3], we outlined the sequence in which inelastic deformation evolved at RT, and it was shown that reaction-zone cracks (see Figure 12a) played an important role in nucleating slip bands during the micro-yield regime of deformation. Although such detailed analyses were not performed for the specimens tested at 538 C, many of the diffused slip bands appeared to originate from reaction-zone cracks, indicating that those cracks also play an important role during elevated temperature deformation. The density of reaction-zone cracks were found to be less at 538 C compared with RT. A possible reason may be some toughening of the reaction-zone at elevated temperatures. Note that the reaction-zone essentially consists of a high volume fraction of titanium silicides and carbides in the base Ti-alloy, and the overall toughness/ductility of that particulate system could increase with temperature. More recent studies [11] indicate that reaction-zone cracks play a very important role in fatigue of MMCs.

Final fracture of the 0° MMC at 538 C occurred through a fiber fracture mechanism, where the critical strength of the fibers were reached; this was similar to the case of RT deformation.

3.2.2 $[90]_8$ MMC

Figures 13a and 13b provide comparisons of the deformation behavior of the $[90]_8$ MMC at RT and 538 C. The figures show that the deformation mechanisms were similar at both temperatures, involving a combination of fiber-matrix debonding (db) at the top and bottom of fibers (i.e., those points along the loading line), and plasticity of the matrix at angles between 30 and 120 degrees with respect to the pole (or loading direction). Also, most of the slip bands were associated with reaction-zone cracks (rzc), although slip bands originating from grain boundaries also were observed. The main difference in the deformation mechanism at the two temperatures was once again with respect to the slip character: planar and sharp slip bands at RT compared with diffused slip at 538 C.

Final failure of the $[90]_8$ MMC at both temperatures involved matrix cracks nucleating within intense slip bands between fibers, and the growth of those cracks along the slip bands. Some delamination damage also was observed. Figure 13c illustrates the microstructure next to the fracture surface for a specimen pulled to failure at RT. The arrows indicate the shear cracks that developed within the intense slip bands.

3.2.3 $[\pm45]_{2s}$ MMC

Figures 14a and 14b illustrate the microstructures of the $[\pm45]_{2s}$ MMC deformed at RT and 538 C, respectively; the former was strained to approximately 5 percent, whereas the latter was unloaded at a strain of approximately 2 percent. Only the edge-view of fibers is presented here. The primary features of deformation at both temperatures included fiber-matrix debonding and slip band formation, similar to those observed for the $[90]_8$ MMC.

Figures 15a and 15b are higher magnification micrographs of $[\pm45]_{2s}$ samples that were pulled to strains of 0.4 percent (within Stage II) and 5 percent (Stage III), respectively, at RT. The arrows indicate that debonding had already started in Stage II, consistent with observed increases in specimen compliance and decreases in Poisson's ratio in Stage II. Only very few slip bands are observed in Figure 15a. On the other hand, Figure 15b shows profuse slip bands, with many of them originating from reaction-zone cracks. In some cases, intense slip activity between fibers produce significant distortion of the matrix around specific fibers. Matrix cracks nucleated within the slip bands and finally led to failure, although their propagation was hindered somewhat by the fibers in the adjacent ply.

Figure 15c shows the microstructure parallel to the face of the specimen, which was strained to approximately 5 percent at RT. The figure shows local necking type behavior and profuse slip activity of the matrix between the fibers.

3.2.4 $[0/90]_{2s}$ MMC

Figure 16a, 16b, and 16c are a series of three photographs that illustrate the microstructures of three $[0/90]_{2s}$ specimens loaded to strains of 0.37 percent, 0.75 percent, and 1.03 percent, respectively, at room temperature. Together they describe the sequence in which inelastic deformation evolved for this system. Reference [7] provides a good description of the finite-element results for this system, backed with mechanical data and microstructural observations; theoretical predictions of the plastic enclaves at different applied strain levels are also provided. The slip band features in Figure 16 are consistent with those results, particularly the fact that plasticity surrounding the 0-degree fiber occurred at axial positions midway between two adjacent 90-degree fibers.

At low strains, Figure 16a shows that most of the slip bands were concentrated at the top and bottom of fibers, similar to the case of the $[90]_8$ MMC [1-5]. Although fiber-matrix debonding is not obvious in the photograph, we suspect that it was present, but became closed when the external load was removed. Figure 16b shows slip bands for both the 0° and 90° plies, and their orientation and nucleation sites are similar to those observed for the unidirectional composites. Examination at higher magnification revealed that many of these slip bands had their origin in reaction-zone cracks at the fiber-matrix interface. In Figure 16b, it is also interesting to note the apparently greater fiber-matrix separation along directions perpendicular to the loading axis than parallel to the loading axis, in direct contrast to the case of the $[90]_8$ system. We believe that this was so because the matrix between the 90° and 0° fibers plastically deformed (see Figure 16) under load, and became thinner; on unloading, the stiff fibers contracted and retained their original position, forcing fiber-matrix separation to occur in the 90-degree plies. The elastic contraction of the 0° fibers also produced a compressive force on the 90° plies, thus closing the normal fiber-matrix debonds (a the top and bottom of fibers) which must have been present in the loaded condition.

4. COMPARISONS OF THEORY WITH EXPERIMENTS

In this section we present a preliminary assessment of how different constitutive models performed in predicting the stress-strain behavior of the $[0]_8$, $[90]_8$, and $[\pm 45]_{2s}$ MMC. Three constitutive models were considered for comparisons: (i) METCAN, developed at NASA Lewis by Chamis et al.[11-13], (ii) AGLPLY, based on the analysis of Dvorak et al.[14], and (iii) a unit-cell finite element method (FEM) model developed at Battelle by Brust et al.[15].

The METCAN computer code [11-13] uses a composite micro-mechanics approach and laminate theory to model the MMC response. It treats the material nonlinearity at the constituent level, where the material's non-linear time-temperature-stress dependence is modeled using power-law type multifactor interaction relationships. Although the model can account for interface damage in a limited way, by changing the mechanical properties of the interphase region (the region consisting of the reaction-zone and the interfaces), it cannot predict *a priori* what the interphase property should be. An additional problem lies in predicting gradual increases in compliance of the $[90]_8$ MMC when it is deformed in Stage II; modeling this would require a growth law that continually changed the interphase property during loading. On the other hand, the main advantage of the METCAN analysis is its simplicity, and the way it lends itself easily to a wide variety of loading conditions and laminate configurations. We expect the model to perform well for the $[0]_8$ system, but not as well for the $[90]_8$ system, particularly for unloading situations.

The AGLPLY code is based on the elastic-plastic analyses of Dvorak et al.[14]. It is based on a vanishing fiber diameter model, which assumes that the fibers do not influence deformation in the transverse direction. AGLPLY can also be conveniently applied to laminate systems. However, its primary drawback is that it cannot account for damage. Once again we expect the model to perform well for the $[0]_8$ system, but not as well for the $[90]_8$ system.

The unit-cell FEM model of Brust et al. [15] is similar to the model of Nimmer et al. [16]. The 2-D unit cell consists of a quarter of the fiber, surrounded by a rectangular matrix. The rectangular boundaries retain their straight faces during deformation, and both in-plane loads and out-of-plane loads (parallel to the fiber direction) can be handled. Generalized plane strain conditions are assumed, so that the fiber and matrix satisfy iso-strain conditions in the fiber direction. An evidence in support of the generalized plane strain formulation was the experimental fact that the width Poisson's ratio (measured using both strain gages and extensometers) for the $[90]_8$ MMC reduced almost to zero in Stage III. Thus, although the area of contact between the fiber and matrix had reduced considerably due to fiber-matrix debonding, the fibers remained effective in preventing any further contraction of the matrix in the fiber direction; i.e., plane strain conditions were maintained. Additional input to the model included varying the bond strength. A bond strength of zero provided excellent correlation with RT data [2,3], but as will be indicated here, a higher bond strength (~ 85 MPa) appeared to be necessary at 538 C to explain the elevated temperature response of the $[90]_8$ MMC. For high temperature deformation, the following history was imposed on the unit cell: (i) cool down from 815 C (processing temperature) with HIP-pressure, (ii) removal of HIP pressure, (iii) heat up to 538 C without load, and (iv) application of load. The primary disadvantage of the unit-cell model currently is that it is not a simple PC-code, and also it has not been applied to complex ply lay-ups.

In all the models that were selected here, the appropriate physical and mechanical properties of the constituents were used. Data on base material properties are available in references [1,2,6].

Figures 17a and 17b provide comparisons of the model predictions with experimental data for the 0° MMC at RT and 538 C, respectively. The METCAN code tended to underestimate the stress-strain response at both temperatures, particularly at strains above 0.4 percent; the reason for the underprediction is not known. The AGLPLY analysis provided good correlation with the experimental data at RT; however, in reference [3] it was shown that the AGLPLY model was not able to provide as good a correlation with the Poisson's ratio data for the 0° MMC at RT. The unit cell model provided excellent correlation with the stress-strain data; Figure 17b shows that the predictions and experimental data lie on top of one another. In reference [3] it was shown that the model also provided good correlation with the Poisson's ratio data at RT.

Figures 18a and 18b provide comparisons of the model predictions with experimental data for the $[90]_8$ MMC at RT and 538 C, respectively. At RT, the Stage I-Stage II transition was predicted reasonably well by the METCAN code. However, at higher strains the METCAN code once again underpredicted the stress-strain response. Although not shown in Figure 18a, the METCAN code can predict compliance increases on unloading in Stage II; however, the compliance increase appears to be a one-time effect, and the code does not appear to satisfactorily show continuous compliance increases which were observed experimentally (see Figure 6a). The AGLPLY model predicted the stress-strain response reasonably well up to a strain of 0.6 percent; however, when the code was used, the modulus of the fibers were artificially reduced (to 3 percent of their original value) at the Stage I-Stage II transition. Without this modification, the code would not have provided good stress-strain correlation with experimental data above a strain of 0.2 percent. The unit-cell model (with zero bond strength) provided best stress-strain correlation with the experimental data at RT. The loading-unloading response was predicted extremely well (see Figure 18a). Figure 18c, from reference [3], shows that the unit-cell model was also able to satisfactorily predict the Poisson's ratio at RT.

At 538 C, the METCAN code over-predicted the Stage I-Stage II transition of the $[90]_8$ MMC by approximately 50 MPa, whereas the unit-cell model with zero bond strength grossly under-predicted the Stage I-Stage II transition. In an effort to evaluate the reason for underprediction of the unit-cell model, the bond strength was varied. It was found that a bond strength of 85 Mpa provided best correlation with the experimental data (see Figure 18b, and the line with triangles). The only interpretation we have currently is that the bond strength may increase with temperature. A possible explanation is that the debonding phenomenon is actually a cracking process in the reaction-zone/fiber interface region (along the axis of fibers, see our photographs in reference [1]), and any ductility increase of the reaction-zone with increasing temperature may increase the stress/strains required for such cracking.

Figures 19a and 19b provide comparisons of the model predictions with experimental data for the $[\pm 45]_{2s}$ MMC at RT and 538 C, respectively. At RT, the METCAN code was able to satisfactorily predict the elastic response, but the inelastic response was greatly overpredicted (in Stages II and III). The reason for the over-prediction is not known, although we suspect that the current version of the code may not have adequately accounted for fiber-matrix debonding for this system. Our experimental findings indicate that fiber-matrix debonding is an important issue for all off-axis systems (because of poor bond strength), and constitutive models must account for such effects.

At 538 C, Stage II appears to have started at almost zero stress; additional experiments are, however, necessary to confirm this finding, particularly since the $[90]_8$ MMC indicated that the Stage II debonding started at a stress of approximately 100 MPa at 538 C. The METCAN code once again overpredicted the stress-strain response. This over-prediction may also be related to inadequate accounting of fiber-matrix debonding in the current version of the METCAN code.

5. DISCUSSION

The stress-strain responses at elevated temperatures for all the lay-ups were similar to those at RT. The effects of elevated temperature were primarily in terms of the reduction of "yield" and failure strengths, and the strains at which they occurred. The similarities of the stress-strain responses suggest that a good understanding of RT deformation behavior (where experiments are simpler to perform) can provide very useful insights into mechanisms that may operate at elevated temperatures.

Two important ways in which a higher temperature can influence the mechanical response include: (i) reduction in elastic modulus and flow stress of the matrix, and (ii) changes in thermal residual stresses (primarily less compressive stress in the fiber along its axis) in the MMC. Fiber-matrix bond strength may also change with temperature, although additional experiments are necessary to evaluate such effects. We believe that all these factors contributed to the differences in the mechanical responses at RT and 538 C.

Time-dependent deformation is also an important issue in high temperature deformation. The Stage I-Stage II transition for the $[90]_8$ MMC increased with strain-rate, indicating a possible role of localized plasticity during the initial period of fiber-matrix debonding. Under constant load creep situations, the strain-rate of the $[0]_8$ MMC decreased as a power-law function of time. Additional experiments are necessary to establish the applicability of this type of relationship. Calculations using a simple one-dimensional model indicated anomalously high creep-rates in the matrix of the $[0]_8$ MMC compared with that of the unreinforced material. The reason for high creep rates are not clear at present, and additional experiments and evaluations are necessary both for confirming the behavior and finding a suitable explanation. Creep experiments with the $[90]_8$ MMC showed that significant creep could occur at stresses as low as 28 MPa, which was lower than the Stage I-Stage II transition stress (approximately 100 MPa) in a simple tension test at 538 C. The unloading data for specimens that were creep tested at stresses lower than the Stage I-Stage II transition stress showed compliance increases associated with creep, indicating that debonding was in progress at such low values of applied stress. These creep results imply that time-dependent plasticity can initiate fiber-matrix debonding well below the macroscopic transition ("yield") stress, and that it may be prudent to assume a zero transition stress for design calculations at elevated temperatures.

With regard to the mechanism of deformation, in references [1-5] we had indicated that the primary mode of deformation of the $[0]_8$ MMC at RT was matrix plasticity. At low strains (in the micro-yield regime of deformation) reaction-zone cracks played an important role in nucleating micro-slip bands, and at larger strains more conventional grain boundary dislocation sources became active. The results presented here on elevated temperature deformation show that inelastic deformation of the $[0]_8$ MMC was once again dominated by matrix plasticity; hardly any fiber or matrix cracks were observed. However, at 538 C the slip was diffused, rather than the planar and sharp slip bands characteristic of RT deformation. This behavior was consistent with the expectation that cross-slip would occur easily at lower stresses at elevated temperatures and reduce the tendency for planar slip. The density of reaction-zone cracks also were found to be less at 538 C compared with RT, and a possible explanation may lie in greater ductility of the reaction-zone at elevated temperatures. Final fracture of the $[0]_8$ MMC at 538 C occurred through a fiber fracture mechanism, where the critical strength of the fibers were reached; this was similar to the case of RT deformation. However, whereas Mo ribbons appeared to influence fiber fracture at RT [1,2], the same appeared not to be the case at 538 C. At 538 C we did observe a Kirkendall type of porosity (resulting from non-uniform diffusion of species, primarily the Mo into Ti) in Mo ribbons in one test, and we are not certain at present whether that effect represents general behavior, or whether the specimen may have been accidentally overheated. Additional experiments may be necessary to confirm the issue of Kirkendall type porosity associated with Mo ribbons.

The deformation mechanisms for the $[90]_8$ MMC were similar at RT and 538 C, involving a combination of fiber-matrix debonding damage (primarily in Stage II), and plasticity (primarily in Stage III). Debonding also was significant for the $[\pm 45]_{2s}$ MMC. Together these imply that debonding is a major deformation mechanism whenever tensile loads are present perpendicular to the fiber direction. Constitutive models must account for such effects. The difference between RT and 538 C deformation was primarily with respect to the slip character: planar slip at RT and diffused slip at 538 C. Many of the slip bands at 538 C were associated with reaction-zone cracks, indicating that they play an important role in nucleating slip; grain boundary dislocation sources were also observed at 538 C.

Comparisons of various models with the experimental data indicated that further refinements were necessary to better predict MMC response at elevated temperatures. The METCAN code performed well for certain loading cases, but in other cases it was found to be deficient. This was particularly true of the off-axis laminates, and where unloading was involved. The AGLPLY code also lacked in its ability to incorporate damage. The best MMC predictions were obtained with the unit-cell FEM model, which provided good correlations with loading-unloading and Poisson's ratio data. With this model, the RT response for the $[90]_8$ system was predicted very well with a zero bond strength, but at 538 C the Stage I-Stage II transition stress could only be predicted if a bond strength of 85 MPa was assumed. We are unable to explain this behavior at present, except to suggest that the bond strength may increase with temperature because of possible ductility increases of the reaction-zone; one indirect evidence in support of the ductility issue is the fact that the $[0]_8$ MMC showed less reaction-zone cracks at 538 C compared with RT. However, additional detailed analysis are certainly needed to understand the source of higher bond strength at elevated temperatures.

6. CONCLUSIONS

The following conclusions may be drawn based on the work presented here:

(i) The stress-strain response was similar at RT and 538 C for all the laminates studied. Thus, at both temperatures there was a two-stage elastic-plastic type of response for the 0° MMC, and a three-stage response for the $[90]_8$ and $[\pm45]_{2s}$ MMC. Consequently, a good understanding of the RT inelastic deformation behavior (where experiments are simpler) can provide useful insights into high temperature deformation characteristics.

(ii) The primary differences in the mechanical response at different temperatures, for all the laminates studied, were the levels of stresses and strains corresponding to the different regimes of deformation, and failure. These differences can be attributed primarily to two factors: (i) reduced flow stress of the matrix at elevated temperatures, and (ii) changes in residual stress pattern in the MMC with increasing temperatures.

(iii) Inelastic deformation of the $[0]_8$ MMC at elevated temperatures was dominated by plasticity, similar to the case of RT deformation. The primary differences were less reaction-zone cracks and diffused slip at elevated temperatures, compared with more reaction-zone cracks and planar concentrated slip at RT. Mechanical data in the form of specimen compliance and Poisson's ratio also pointed to plasticity being the dominant inelastic deformation mechanism at both temperatures.

(iv) Inelastic deformation of the $[90]_8$ and $[\pm45]_{2s}$ MMC involved a combination of plasticity and damage at both temperatures. The main effect of temperature was that the slip character changed from planar slip to diffused slip in going from RT to elevated temperatures. Mechanical data in the form of compliance increases and Poisson's ratio decreases also pointed to damage being significant in the off-axis MMCs.

(v) Comparisons of model predictions with experimental data showed that both the METCAN and AGLPLY codes needed refinements for predicting the mechanical response of off-axis systems. The unit-cell FEM model provided best correlation with the stress-strain, loading-unloading, and Poisson's ratio data for the unidirectional $[0]_8$ and $[90]_8$ systems. The high temperature mechanical response suggested that the fiber-matrix bond strength may increase with temperature. The basis for this remains to be examined in detail.

7. ACKNOWLEDGMENTS

This work was supported by the NASA-Lewis Research Center, under contract number NAS3-26053 through the HITEMP program. We specially thank our monitor, Dr. J. Rod Ellis of NASA Lewis, for his constant encouragement and guidance throughout this program. We would also like to acknowledge the many useful discussions with Drs. B. Lerch and Steve Arnold of NASA Lewis, and the data they provided for use in this work. We thank Dr. F.W. Brust of Battelle for providing results of the elastic-plastic-damage FEM analysis related to the unit-cell model. Finally, we thank Mr. N. Frey, Mr. G. Foster and Mr. G. Clark of Battelle and Mr. Hendrick Coljin of Ohio State University for their superb experimental support during this program.

8. REFERENCES

1. B.S. Majumdar and G.M. Newaz, "Inelastic Deformation of Metal Matrix Composites", Part I of Final Report to the NASA Lewis Research Center, to be published as a NASA Contractor Report (September 1991)

2. B.S. Majumdar,"Inelastic Deformation of Metal Matrix Composites: Plasticity and Damage Mechanisms", Philosophical Magazine, in press (1992)

3. B.S. Majumdar, G.M. Newaz, and J.R. Ellis,"Evolution of Damage and Plasticity in Titanium Based Fiber Reinforced Composites", submitted to the Metall. Trans. (1992)

4. B.S. Majumdar and G.M. Newaz,"Inelastic Deformation of Metal Matrix Composites", Proceedings of the 1991 HITEMP Conference at NASA Lewis, NASA Technical Publication TM10082, pp.34.1-34.16 (1991)

5. G.M. Newaz and B.S. Majumdar,"Deformation and Failure Mechanisms in Metal Matrix Composites", Proceedings of the ASME Winter Annual Meting, Atlanta, Georgia, AD Vol.22 (1991)

6. B.A. Lerch and J.F. Saltsman,"Tensile Deformation and Damage in SiC Reinforced Ti-15V-3Cr-3Al-3Sn", NASA Technical Memorandum 103620 (1991)

7. B.A. Lerch, M.W. Melis, and M. Tong,"Experimental and Analytical Analysis of Stress-Strain Behavior in a $[90°/0°]_{2s}$, SiC/Ti-15-3 Laminate", NASA Technical Memorandum 104470 (1991)

8. W.S. Johnson, S.J. Lubowinski, and A.L. Highsmith, "Mechanical Characterization of Unnotched SCS6/Ti-15-3 Metal Matrix Composites at Room Temperature", Thermal and Mechanical Behavior of Metal Matrix and Ceramic Matrix Composites, ASTM STP1080, Ed. H.H. Moller and W.S. Johnson, ASTM, Philadelphia, pp.193-218 (1990)

9. M.E. Tuttle and J. Rogacki,"Thermo-Plastic Response of Ti-15-3 Under Various Loading Conditions", NASA Contractor Report 187621 (1991)

10. S. Goto and M. McLean,"Role of Interfaces in the Creep of Fiber-Reinforced Metal Matrix Composites - I Continuous Fibers", Acta Metall. Vol. 39, pp.153-164 (1991)

11. C.C. Chamis and D.A. Hopkins,"Thermo-Viscoplastic Nonlinear Constitutive Relationships for Structural Analysis of High-Temperature Metal Matrix Composites", Testing Technology of Metal Matrix Composites, Ed. P.R. Giovanni and N.R. Adsit, ASTM STP 964, pp.177-196 (1988)

12. H.J. Lee, P.L.N. Murthy, and C.C. Chamis, METCAN Updates for High Temperature Composite Behavior: Simulation/Verification, NASA Technical Memorandum 103682 (1991)

13. S.K. Mital and H.J. Lee,"Computational Simulation of Matrix Microslip Bands in SiC/Ti-15 Composite", Proceedings of the 1991 HITEMP Conference at NASA Lewis, NASA Technical Publication TM10082, pp.35.1-35.9 (1991)

14. G.J. Dvorak and Y.A. Bahei-El-Din, J. Appl. Mech., Vol.49, pp.327-335 (1982)

15. F.W. Brust, B.S. Majumdar, and G.M. Newaz,"Constitutive Response Analysis of Metal Matrix Composites via the Unit Cell Model", presented at the ASTM 11th. Symposium on Composite Materials (May, 1992), and to be published as Conference Proceedings

16. R.P. Nimmer, R.J. Bankert, E.S. Russell, G.A. Smith, and K.P. Wright, J. Composite Technology and Research, **13**, 1, pp 3-13 (1991)

LIST OF FIGURES

FIGURE 1. Sketch illustrating domains of *elastic* and *inelastic* deformation for metal matrix composites
FIGURE 2. High temperature test setup, showing longitudinal, width, and thickness strains of the MMC being measured using three extensometers
FIGURE 3a. Stress-strain behavior of 0° MMC specimens, tension tested at 538 C and room temperature. The results from a creep test are also included.
FIGURE 3b. Width strain plotted versus the longitudinal strain for 0° MMC specimens tested at 538 C. The data points are indicated by dots, and the solid lines correspond to best-fit polynomials.
FIGURE 3c. Thickness strain plotted versus the longitudinal strain for a 0° MMC specimen, tension tested at 538 C (1000 F).
FIGURE 4a Stress versus longitudinal strain response from a short-term creep test; 0° MMC, 538 C (1000 F).
FIGURE 4b. Strain versus time behavior for the $[0^{\circ}]_8$ sample in Figure 4a.
FIGURE 5a. Strain-rate plotted versus time for the creep specimen in Figure 4a.
FIGURE 5b. Strain-rate plotted versus the calculated matrix stress, for the 0° specimen creep-tested at 538 C. The MMC data (dots) are also compared with the Ti 15-3 matrix creep data at 566 C (square symbols).
FIGURE 6a. Stress versus longitudinal strain response for the $[90^{\circ}]_8$ system at RT, 538 C (1000 F), and 649 C (1200 F).
FIGURE 6b. Width strain plotted versus the longitudinal strain for a $[90^{\circ}]_8$ specimen tested at 538 C. The dots represent loading-unloading data.
FIGURE 7. Effects of strain-rate on the stress-strain response of the $[90^{\circ}]_8$ system at 538 C (1000 F).
FIGURE 8. Comparisons of the stress-strain response of the $[90^{\circ}]_8$ MMC and the Ti 15-3 matrix at RT and 538 C.
FIGURE 9a. Strain-versus-time behavior for three $[90^{\circ}]_8$ specimens, creep-tested at 538 C.
FIGURE 9b. Stress-strain behavior for three $[90^{\circ}]_8$ specimens, creep-tested at 538 C.
FIGURE 9c. Width strain plotted versus the longitudinal strain for the $[90^{\circ}]_8$ specimen, creep tested at a stress of 69 MPa at 538 C.
FIGURE 10a. Stress-versus-longitudinal strain response for the $[\pm 45^{\circ}]_{2s}$ MMC at RT and 538 C.

FIGURE 10b.	Width strain plotted versus the longitudinal strain for the $[\pm 45^\circ]_{2s}$ specimens.
FIGURE 11a.	Stress-versus-longitudinal strain response for the $[0/90^\circ]_{2s}$ MMC at RT and 538 C.
FIGURE 11b.	Width strain plotted versus the longitudinal strain for the $[0/90^\circ]_{2s}$ specimens tested at RT and 538 C.
FIGURE 11c.	Instantaneous width Poisson's ratio plotted versus the longitudinal strain for the $[0/90^\circ]_{2s}$ specimens tested at RT.
FIGURE 12a.	Microstructure of the $[0^\circ]_8$ specimen, tension tested to failure at RT. Slip bands and reaction-zone cracks are indicated by arrows. Loading axis is horizontal. Magnification 200 X.
FIGURE 12b.	Microstructure of the $[0^\circ]_8$ specimen, tension tested to failure at 538 C. Diffused slip bands are indicated by arrows. Loading axis is horizontal. Magnification 200 X.
FIGURE 13a.	Microstructure of the $[90^\circ]_8$ specimen, tension tested at RT. Sharp slip bands and reaction-zone cracks are indicated by arrows. Loading axis is vertical. Magnification 200 X.
FIGURE 13b.	Microstructure of the $[90^\circ]_8$ specimen, tension tested at 538 C. Diffused slip bands and reaction-zone cracks are indicated by arrows. Loading axis is vertical. Mag. 200 X.
FIGURE 13c.	Region near the fracture surface of a $[90^\circ]_8$ specimen, tension tested to failure at RT. The shearing crack morphology is indicated by arrows. Loading axis is vertical. Mag. 100 X.
FIGURE 14a.	Microstructure of a $[\pm 45^\circ]_{2s}$ specimen, tension tested at RT. Slip bands and reaction-zone cracks are indicated by arrows. Loading axis is vertical. Mag. 100 X.
FIGURE 14b.	Microstructure of a $[\pm 45^\circ]_{2s}$ specimen, tension tested at 538 C. Slip bands and reaction-zone cracks are indicated by arrows. Loading axis is vertical. Mag. 100 X.
FIGURE 15a.	Higher magnification micrograph of a $[\pm 45^\circ]_{2s}$ specimen, tension tested to a strain of 0.4 percent (inside Stage II) at RT. Loading axis is vertical. Mag. 200 X.
FIGURE 15b.	Higher magnification micrograph of a $[\pm 45^\circ]_{2s}$ specimen, tension tested to a strain of 5.5 percent at RT. Loading axis is vertical. Magnification 200 X.
FIGURE 15c.	Longitudinal section of a $[\pm 45^\circ]_{2s}$ specimen, tension tested to a strain of 5.5 percent at RT. Magnification 200 X.

FIGURE 16.	Series of three photographs, illustrating plasticity evolution in the $[0/90^\circ]_{2s}$ system at RT. Figures (a), (b), and (c) correspond to strains of 0.37, 0.75 and 1.03 percent, respectively. Loading axis is vertical. Magnification 200X.
FIGURE 17a.	Comparison of model predictions with experimental data for the $[0^\circ]_8$ MMC at RT.
FIGURE 17b.	Comparison of model predictions with experimental data for the $[0^\circ]_8$ MMC at 538 C.
FIGURE 18a.	Comparison of model predictions with experimental data for the $[90^\circ]_8$ MMC at RT.
FIGURE 18b.	Comparison of model predictions with experimental data for the $[90^\circ]_8$ MMC at 538 C.
FIGURE 18c.	Plot of the instantaneous width Poisson's ratio versus the longitudinal strain for the $[90^\circ]_8$ MMC at RT, showing how the predictions of the AGLPLY code and Battelle's unit-cell FEM model compare with the experimental data.
FIGURE 19a.	Comparison of model predictions with experimental data for the $[\pm 45^\circ]_{2s}$ MMC at RT.
FIGURE 19b.	Comparison of model predictions with experimental data for the $[\pm 45^\circ]_{2s}$ MMC at 538 C.

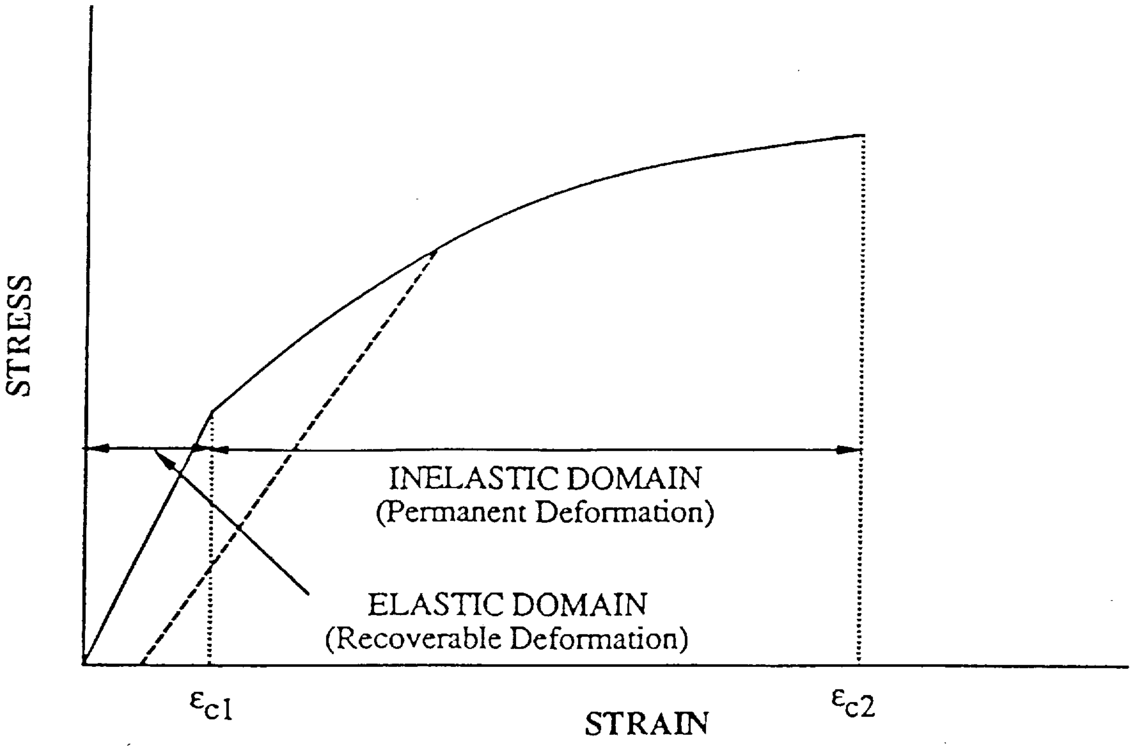

Figure 1. Schematic illustrating typical stress-strain behavior for a fiber-reinforced MMC; ϵ_{c1} and ϵ_{c2} represent strains corresponding to the start of inelastic deformation and composite failure, respectively.

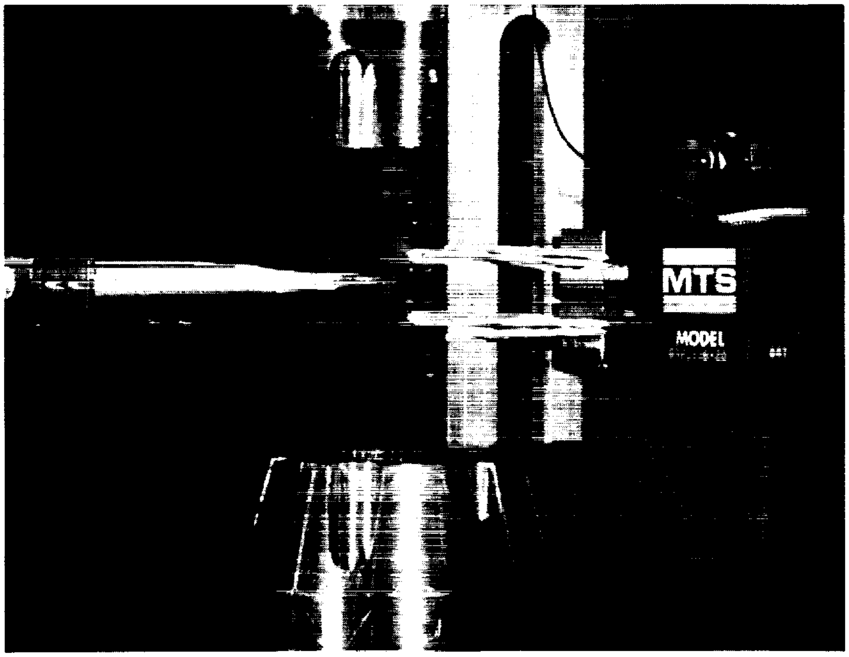

Figure 2. High temperature test setup, showing longitudinal and width strains of the MMC being measured using two extensometers.

ORIGINAL PAGE
BLACK AND WHITE PHOTOGRAPH

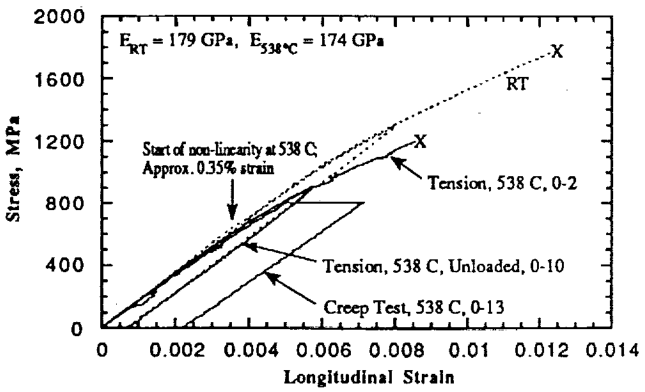

060102010013.plot

Dotted lines correspond to room temperature tests

Figure 3a. Stress-strain behavior of 0° MMC specimens, tension tested at 538 C and room temperature. The results from a creep test are also included.

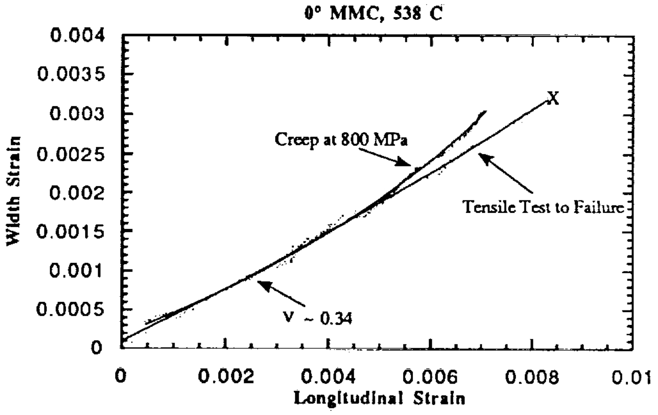

02013wsvsls.plot

Figure 3b. Width strain plotted versus the longitudinal strain for 0° MMC specimens tested at 538 C. The data points are indicated by dots, and the solid lines correspond to best-fit polynomials.

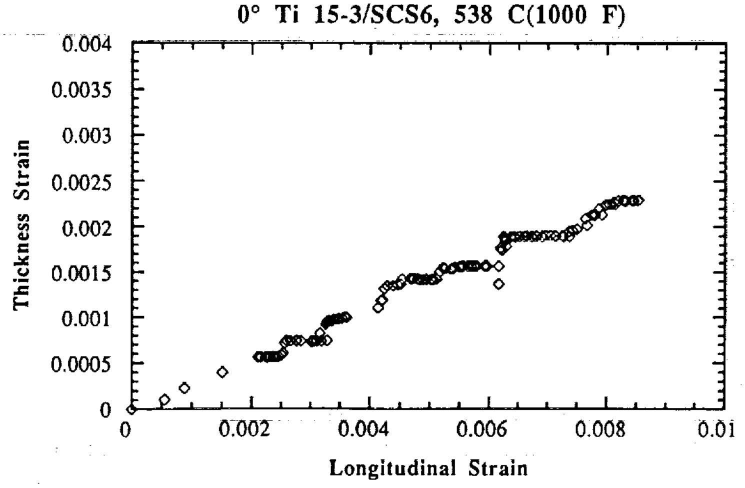

02tsvsls.plot

Figure 3c. Thickness strain plotted versus the longitudinal strain for a 0° MMC specimen, tension tested at 538 C (1000 F).

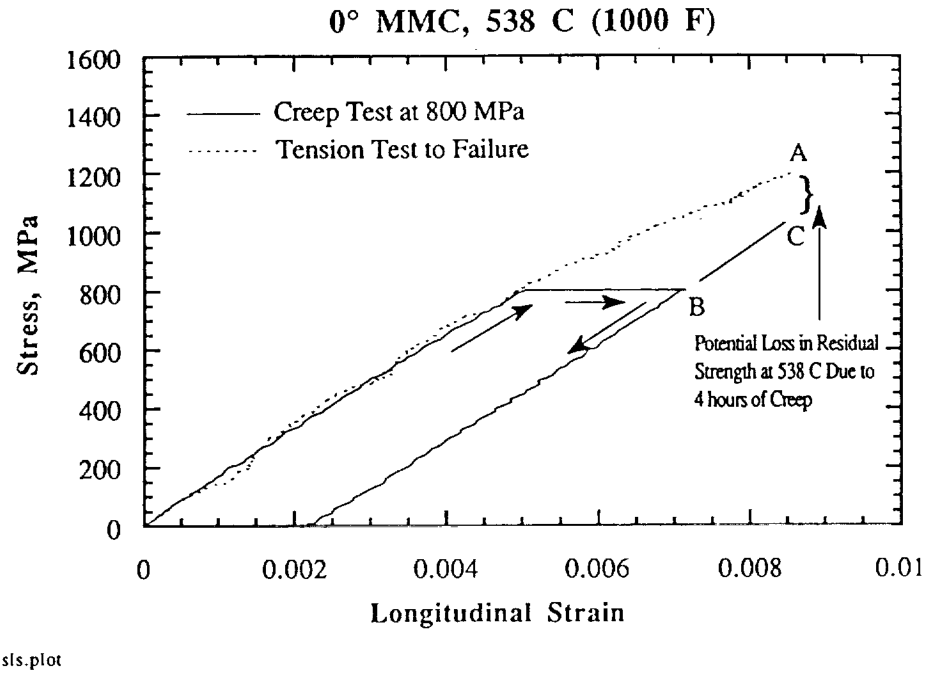

Figure 4a Stress versus longitudinal strain response from a short-term creep test; 0° MMC, 538 C (1000 F).

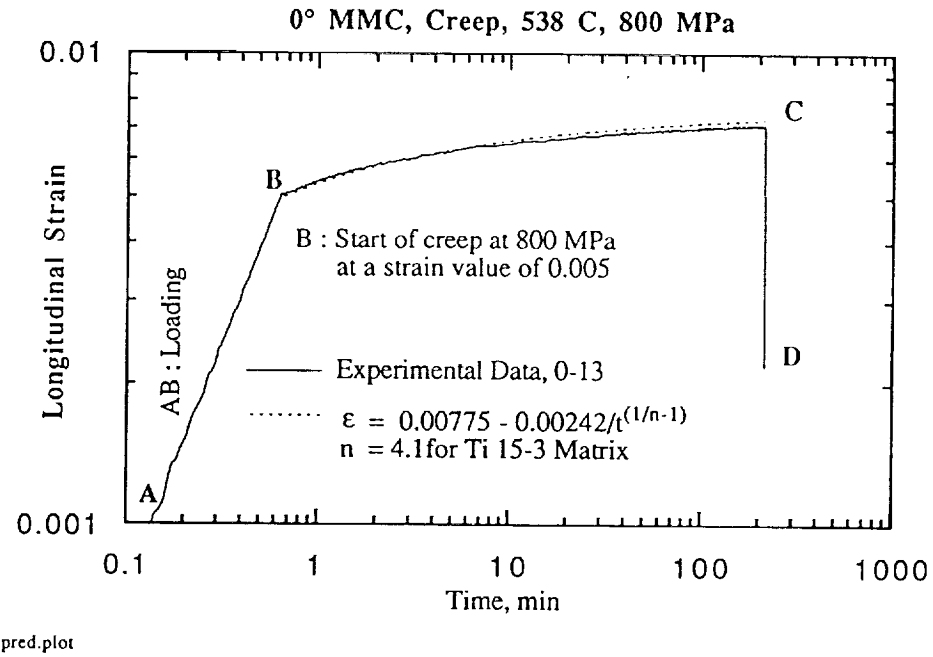

Figure 4b. Strain versus time behavior for the $[0°]_8$ sample in Figure 4a.

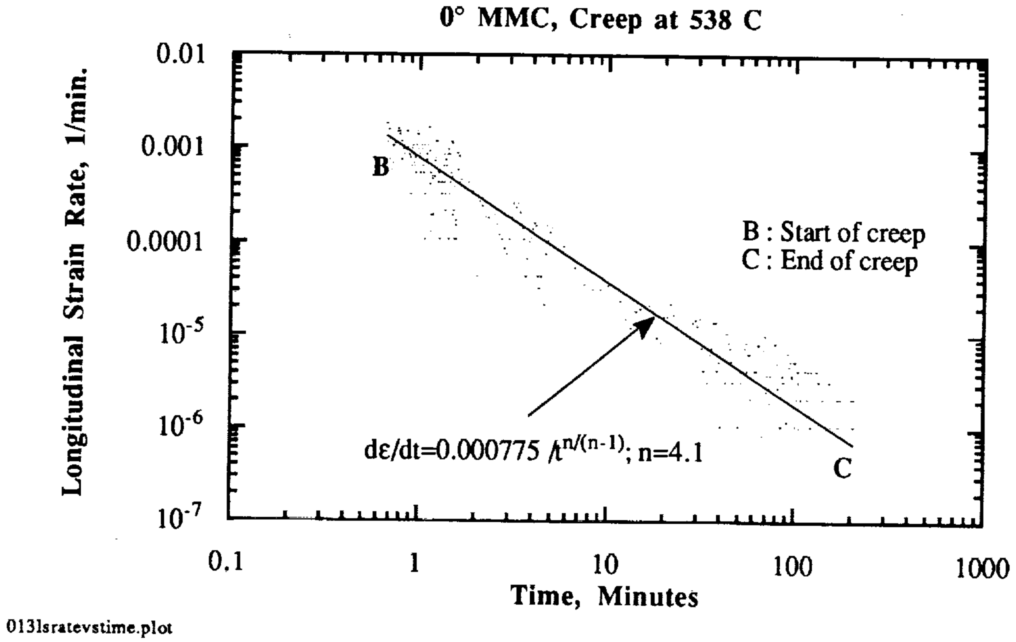

Figure 5a. Strain-rate plotted versus time for the creep specimen in Figure 4a.

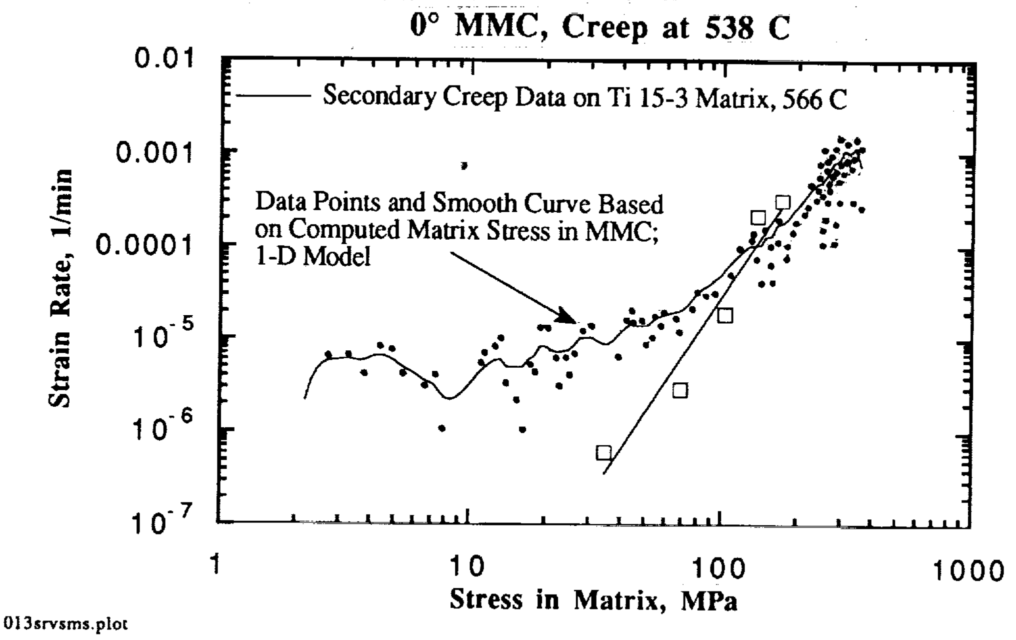

Figure 5b. Strain-rate plotted versus the calculated matrix stress, for the 0° specimen creep-tested at 538 C. The MMC data (dots) are also compared with the Ti 15-3 matrix creep data at 566 C (square symbols).

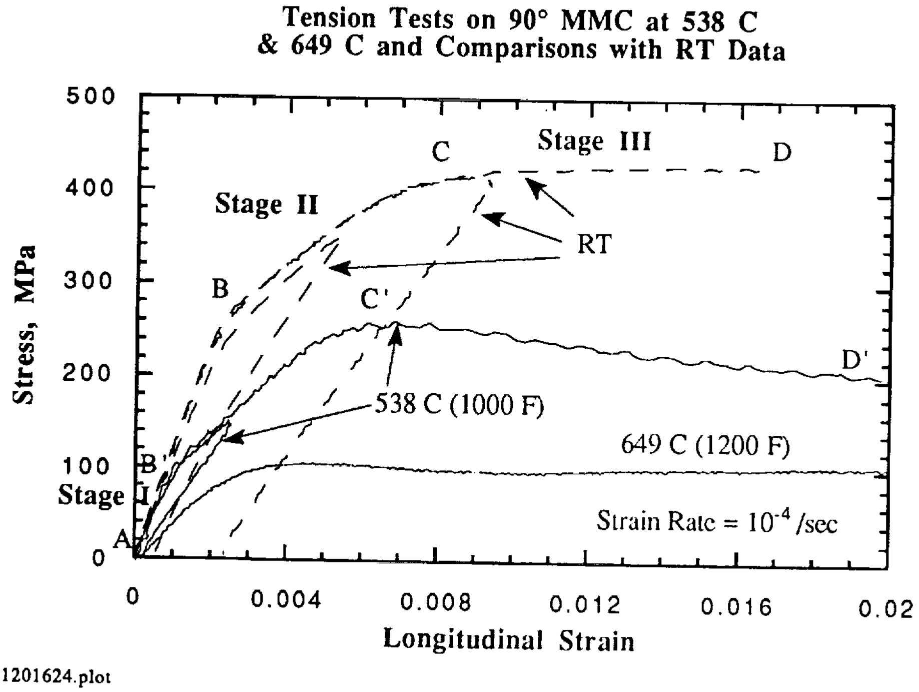

Figure 6a. Stress versus longitudinal strain response for the $[90°]_8$ system at RT, 538 C (1000 F), and 649 C (1200 F).

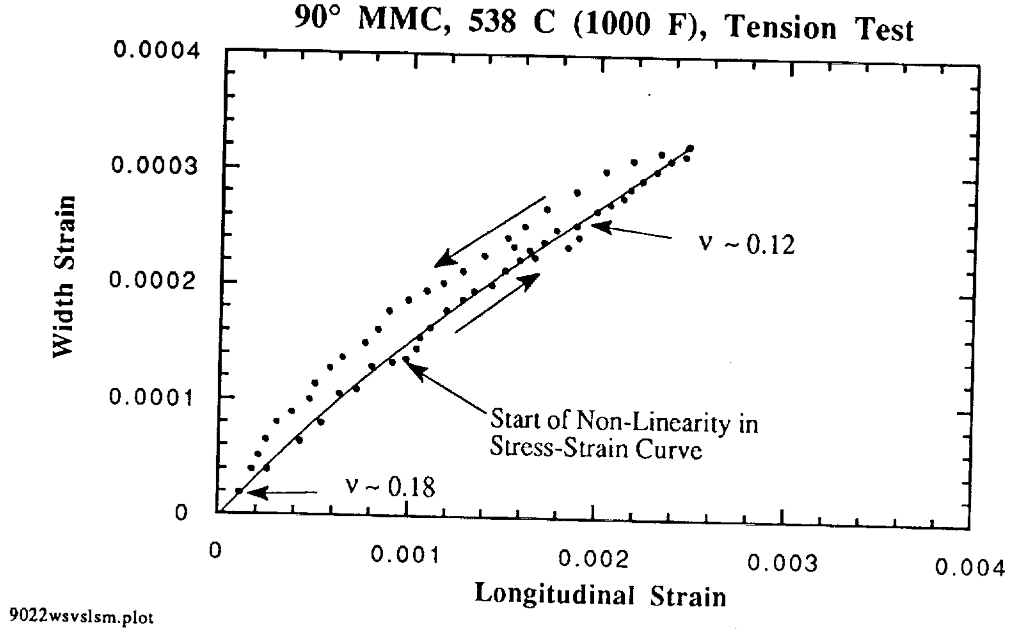

Figure 6b. Width strain plotted versus the longitudinal strain for a $[90°]_8$ specimen tested at 538 C. The dots represent loading-unloading data.

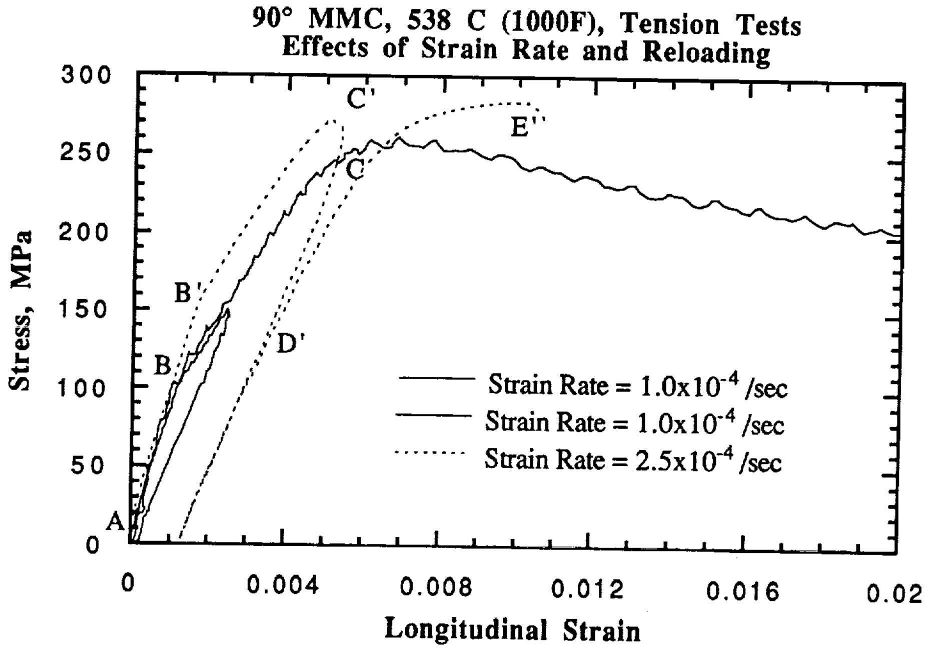

90182226.plot

Figure 7. Effects of strain-rate on the stress-strain response of the $[90°]_8$ system at 538 C (1000 F).

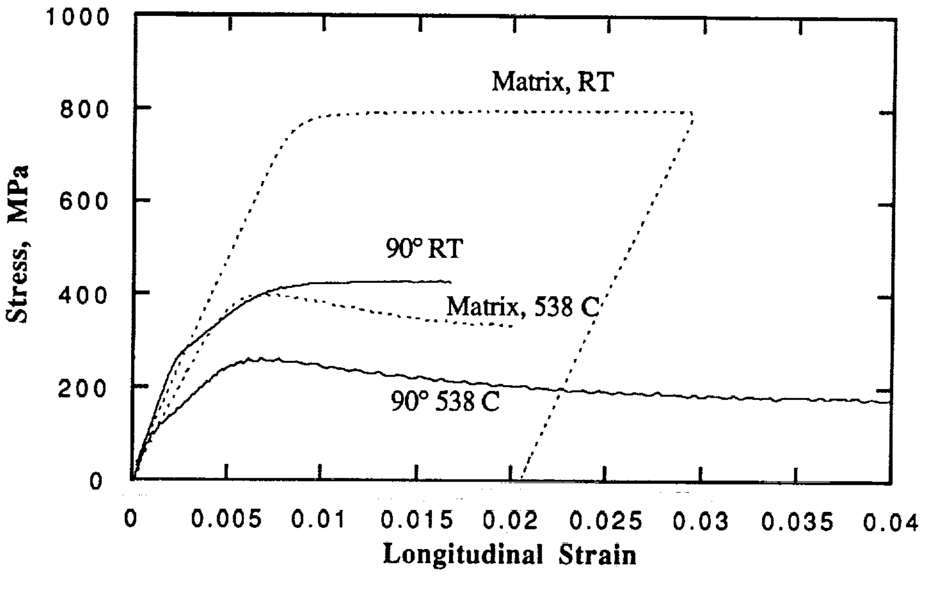

90118M1M3.plot

Figure 8. Comparisons of the stress-strain response of the $[90°]_8$ MMC and the Ti 15-3 matrix at RT and 538 C.

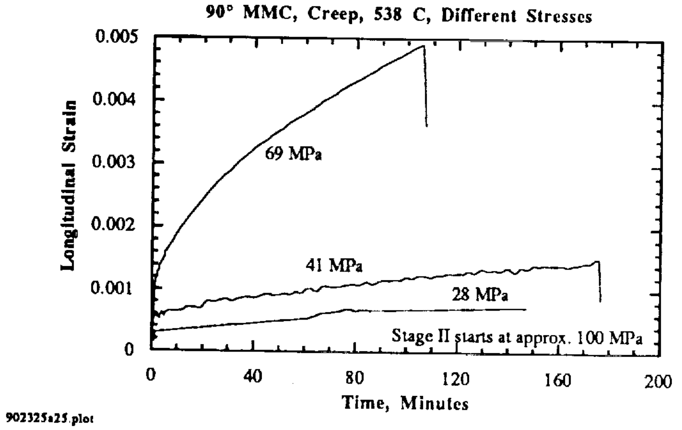

Figure 9a. Strain-versus-time behavior for three $[90°]_8$ specimens, creep-tested at 538 C.

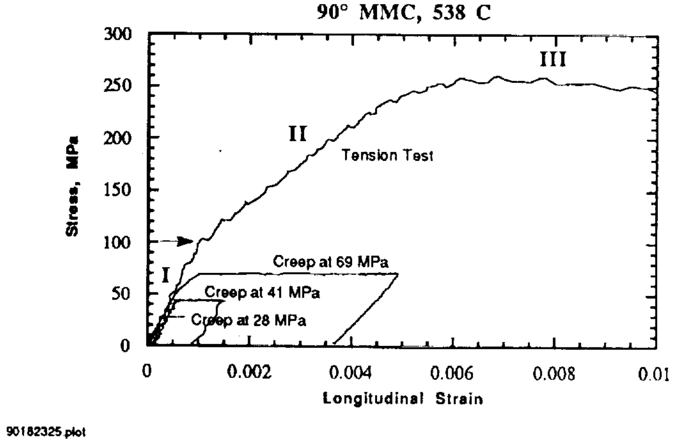

Figure 9b. Stress-strain behavior for three $[90°]_8$ specimens, creep-tested at 538 C.

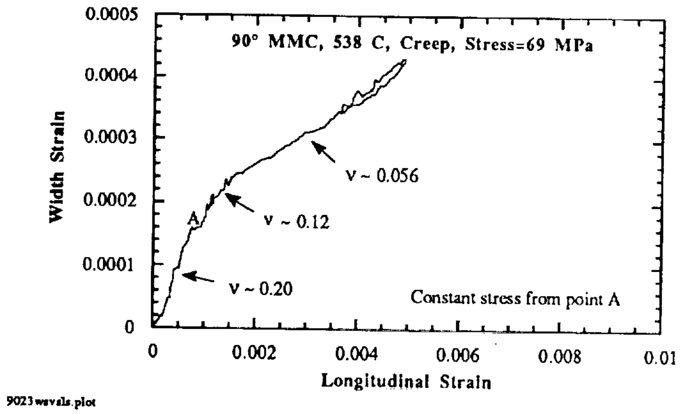

Figure 9c. Width strain plotted versus the longitudinal strain for the $[90°]_8$ specimen, creep tested at a stress of 69 MPa at 538 C.

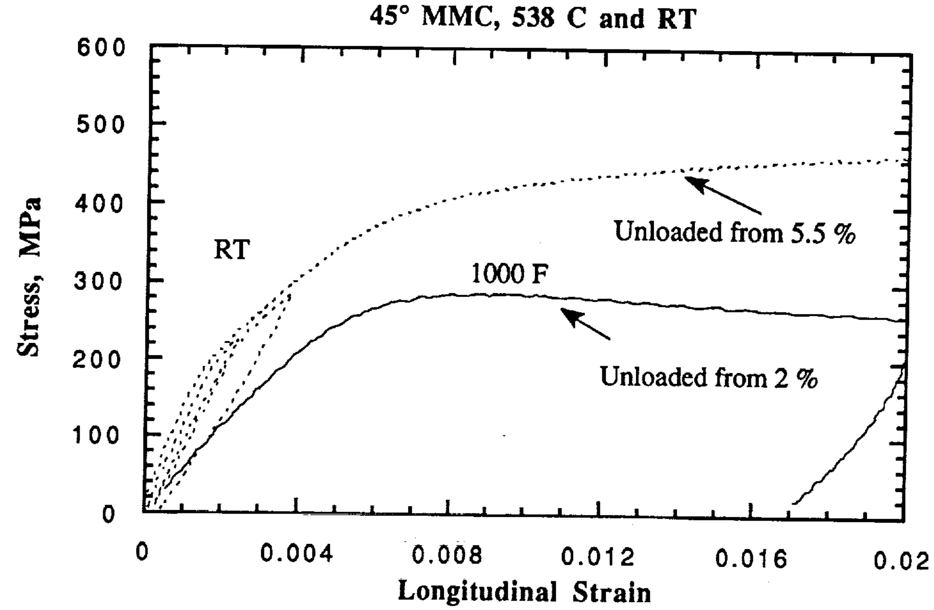

45456strsvsls.plot

Figure 10a. Stress-versus-longitudinal strain response for the [±45°]$_{2s}$ MMC at RT and 538 C.

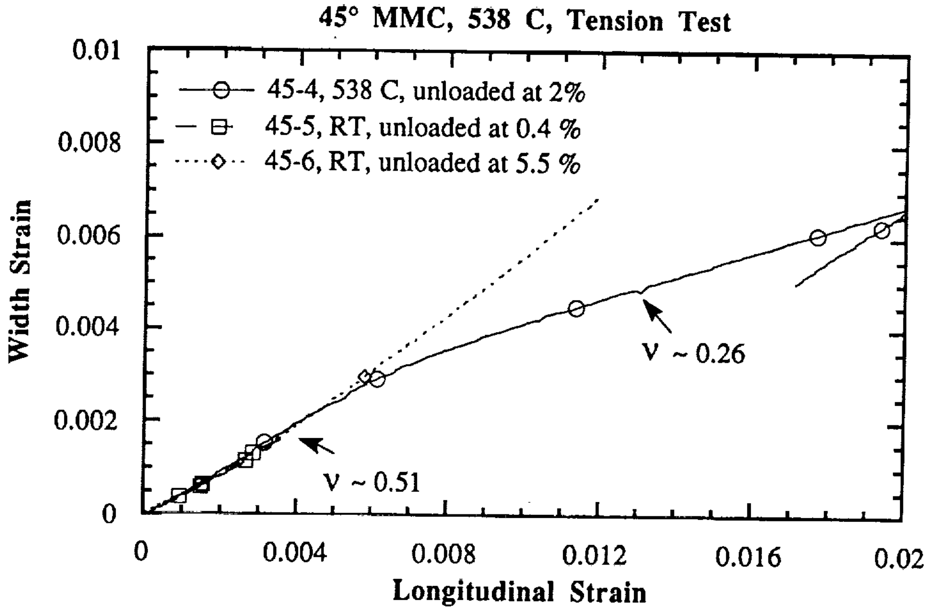

45456wsvsls.plot

Figure 10b. Width strain plotted versus the longitudinal strain for the [±45°]$_{2s}$ specimens.

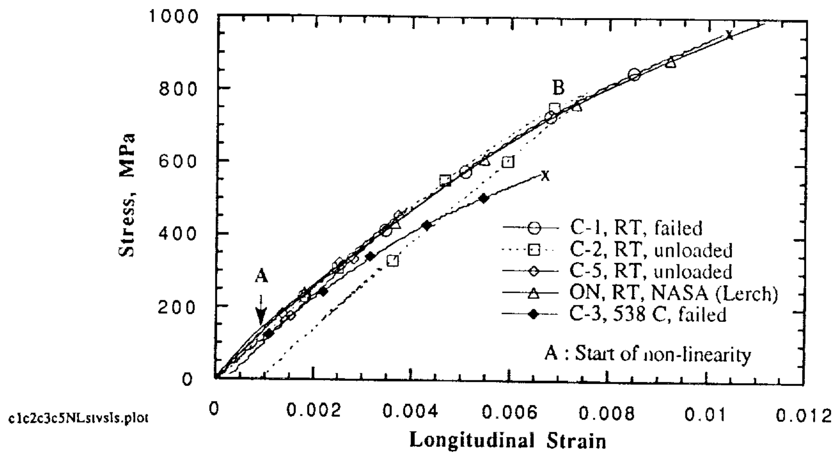

Figure 11a. Stress-versus-longitudinal strain response for the $[0/90°]_{2s}$ MMC at RT and 538 C.

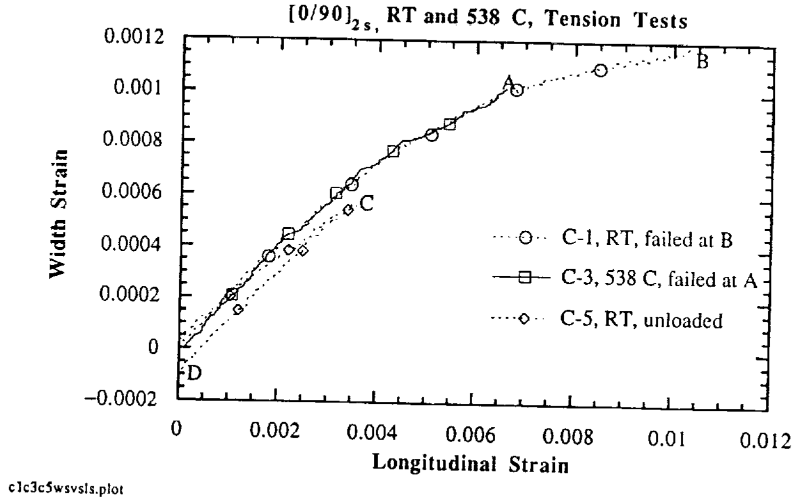

Figure 11b. Width strain plotted versus the longitudinal strain for the $[0/90°]_{2s}$ specimens tested at RT and 538 C.

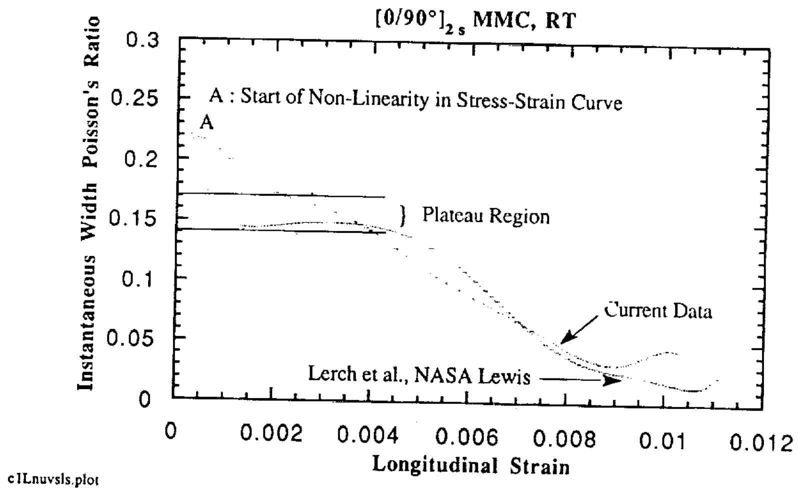

Figure 11c. Instantaneous width Poisson's ratio plotted versus the longitudinal strain for the $[0/90°]_{2s}$ specimens tested at RT.

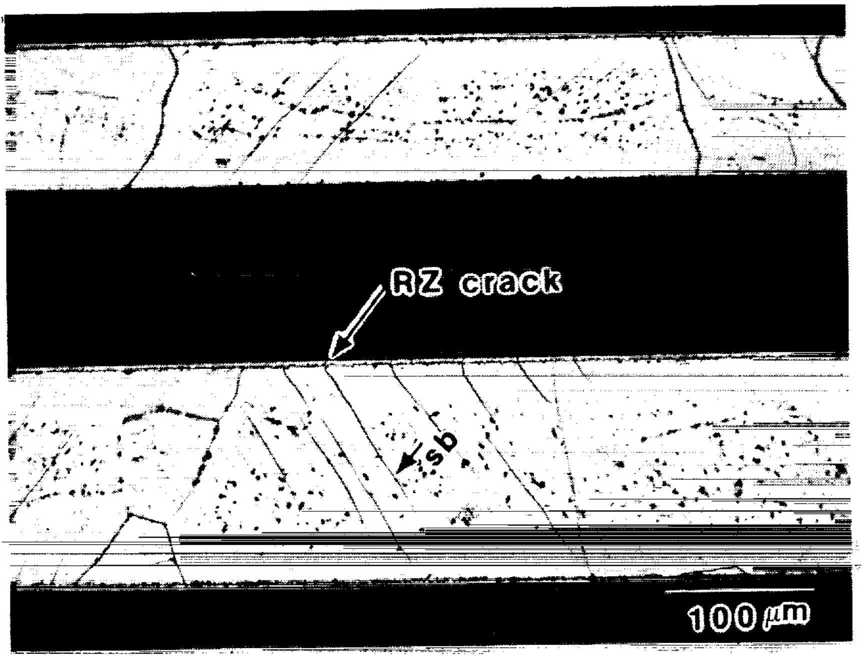

Figure 12a. Microstructure of the $[0°]_8$ specimen, tension tested to failure at RT. Slip bands and reaction-zone cracks are indicated by arrows. Loading axis is horizontal. Mag. 200X.

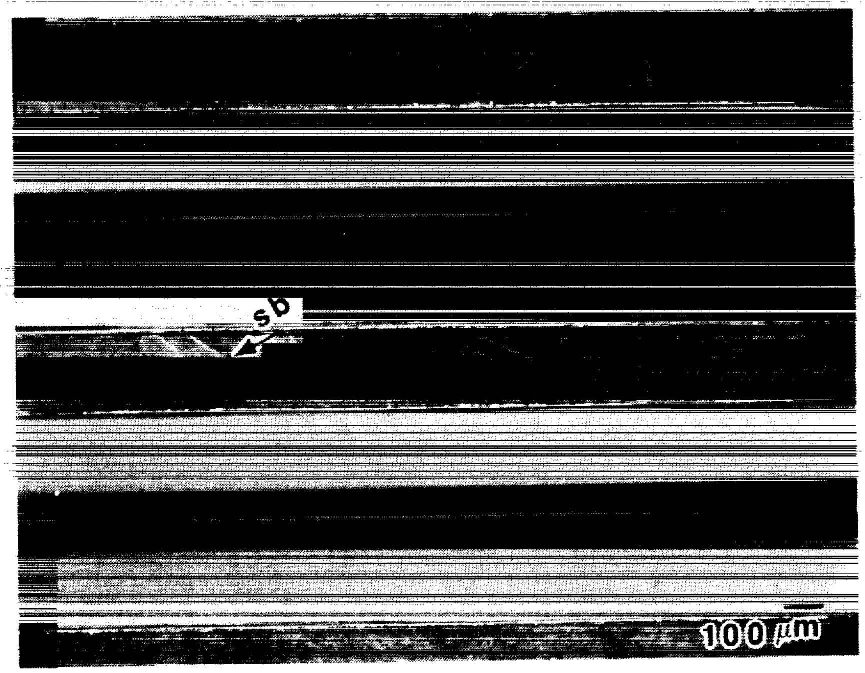

Figure 12b. Microstructure of the $[0°]_8$ specimen, tension tested to failure at 538 C. Diffused slip bands are indicated by arrows. Loading axis is horizontal. Magnification 200X.

ORIGINAL PAGE
BLACK AND WHITE PHOTOGRAPH

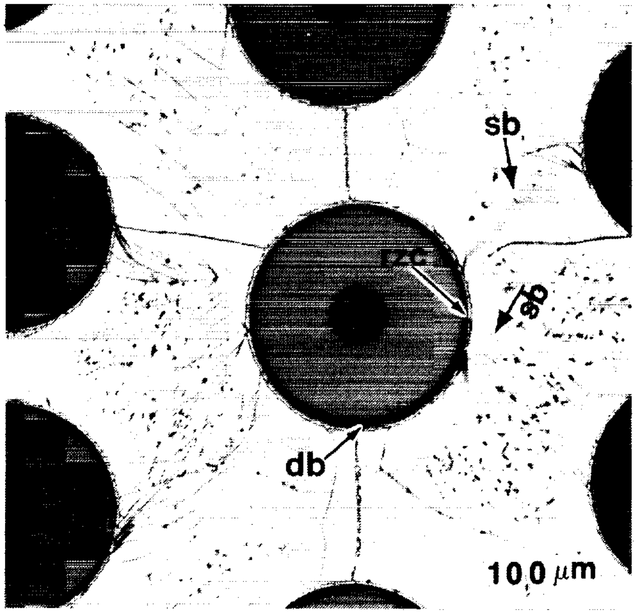

Figure 13a. Microstructure of the $[90°]_8$ specimen, tension tested at RT. Sharp slip bands and reaction-zone cracks are indicated by arrows. Loading axis is vertical. Magnification 200X.

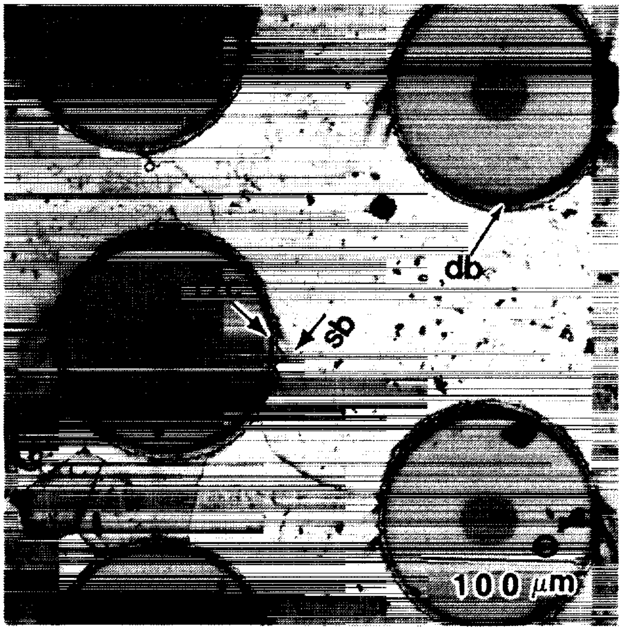

Figure 13b. Microstructure of the $[90°]_8$ specimen, tension tested at 538 C. Diffused slip bands and reaction-zone cracks are indicated by arrows. Loading axis is vertical. Mag. 200X.

ORIGINAL PAGE
BLACK AND WHITE PHOTOGRAPH

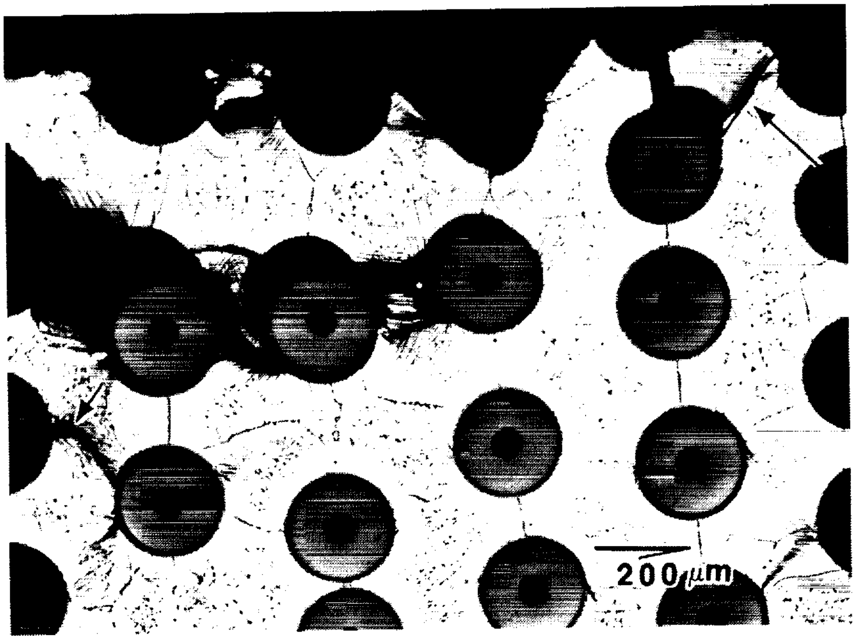

Figure 13c. Region near the fracture surface of a $[90°]_8$ specimen, tension tested to failure at RT. The shearing crack morphology is indicated by arrows. Loading axis is vertical. Mag. 100X.

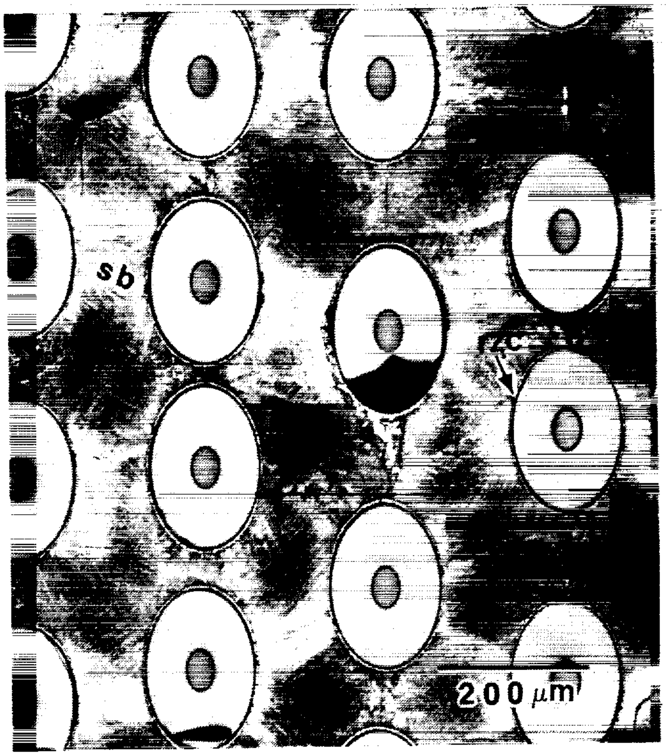

Figure 14a. Microstructure of a $[\pm 45°]_{2s}$ specimen, tension tested at RT. Slip bands and reaction-zone cracks are indicated by arrows. Loading axis is vertical. Magnification 100X.

ORIGINAL PAGE
BLACK AND WHITE PHOTOGRAPH

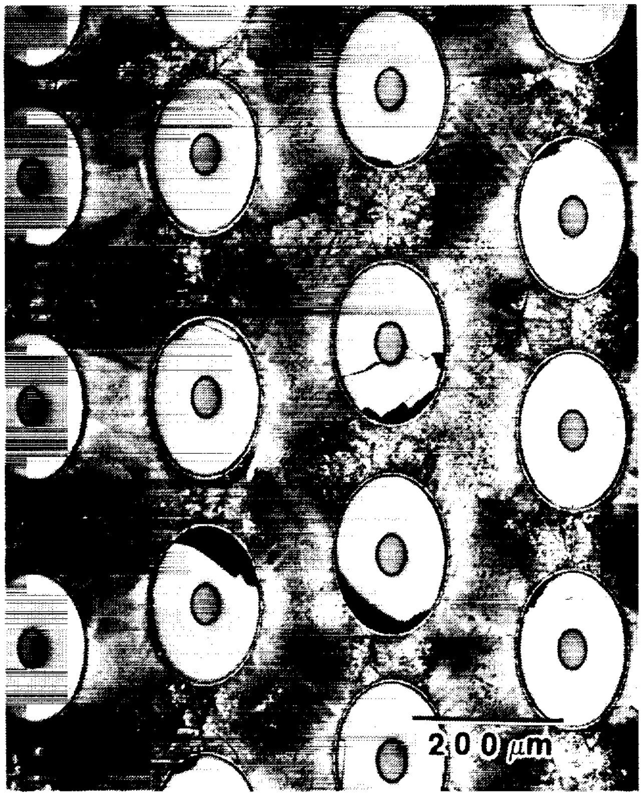

Figure 14b. Microstructure of a $[\pm 45°]_{2s}$ specimen, tension tested at 538 C. Slip bands and reaction-zone cracks are indicated by arrows. Loading axis is vertical Magnification 100X.

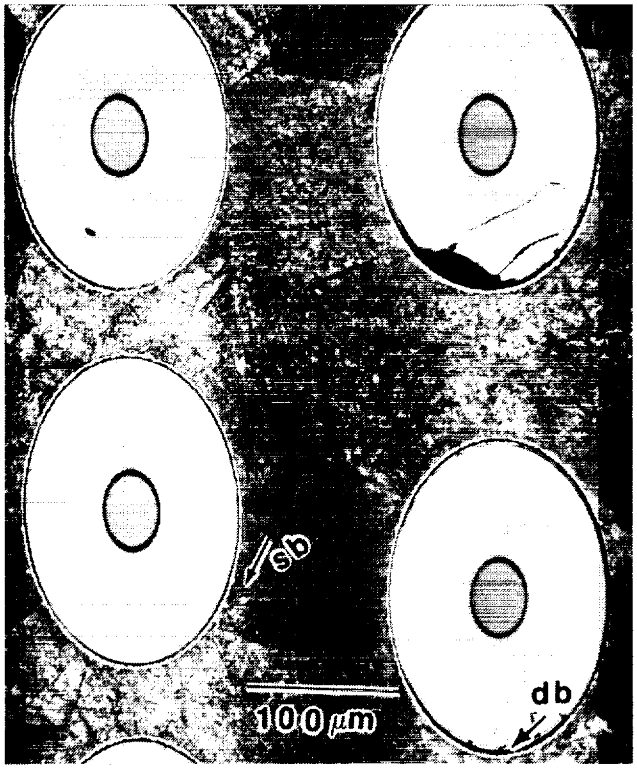

Figure 15a. Higher magnification micrograph of a $[\pm 45°]_{2s}$ specimen, tension tested to a strain of 0.4 percent (inside Stage II) at RT. Loading axis is vertical. Magnification 200X.

ORIGINAL PAGE
BLACK AND WHITE PHOTOGRAPH

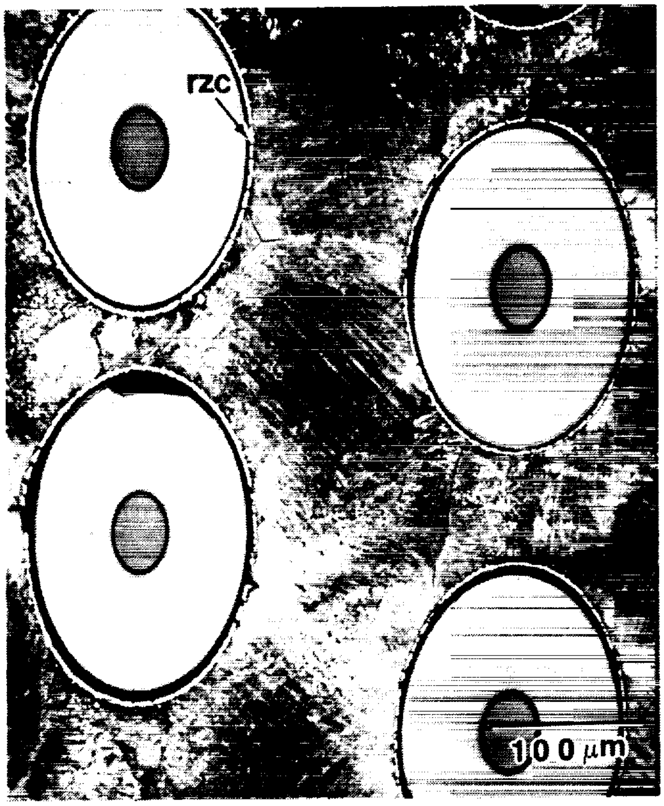

Figure 15b. Higher magnification micrograph of a $[\pm 45°]_{2s}$ specimen, tension tested to a strain of 5.5 percent at RT. Loading axis is vertical. Magnification 200X.

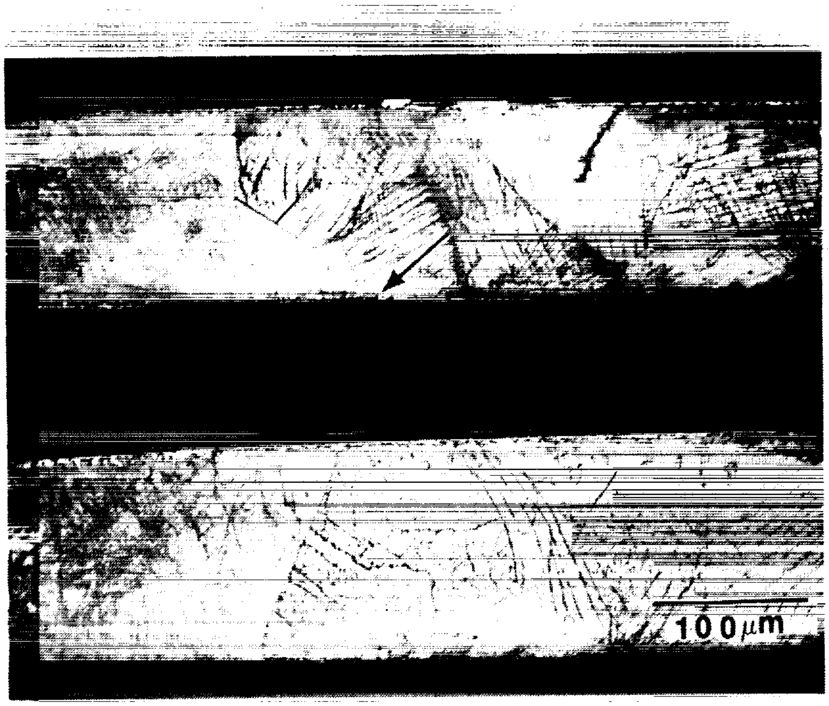

Figure 15c. Longitudinal section of a $[\pm 45°]_{2s}$ specimen, tension tested to a strain of 5.5 percent at RT. Magnification 200X.

ORIGINAL PAGE
BLACK AND WHITE PHOTOGRAPH

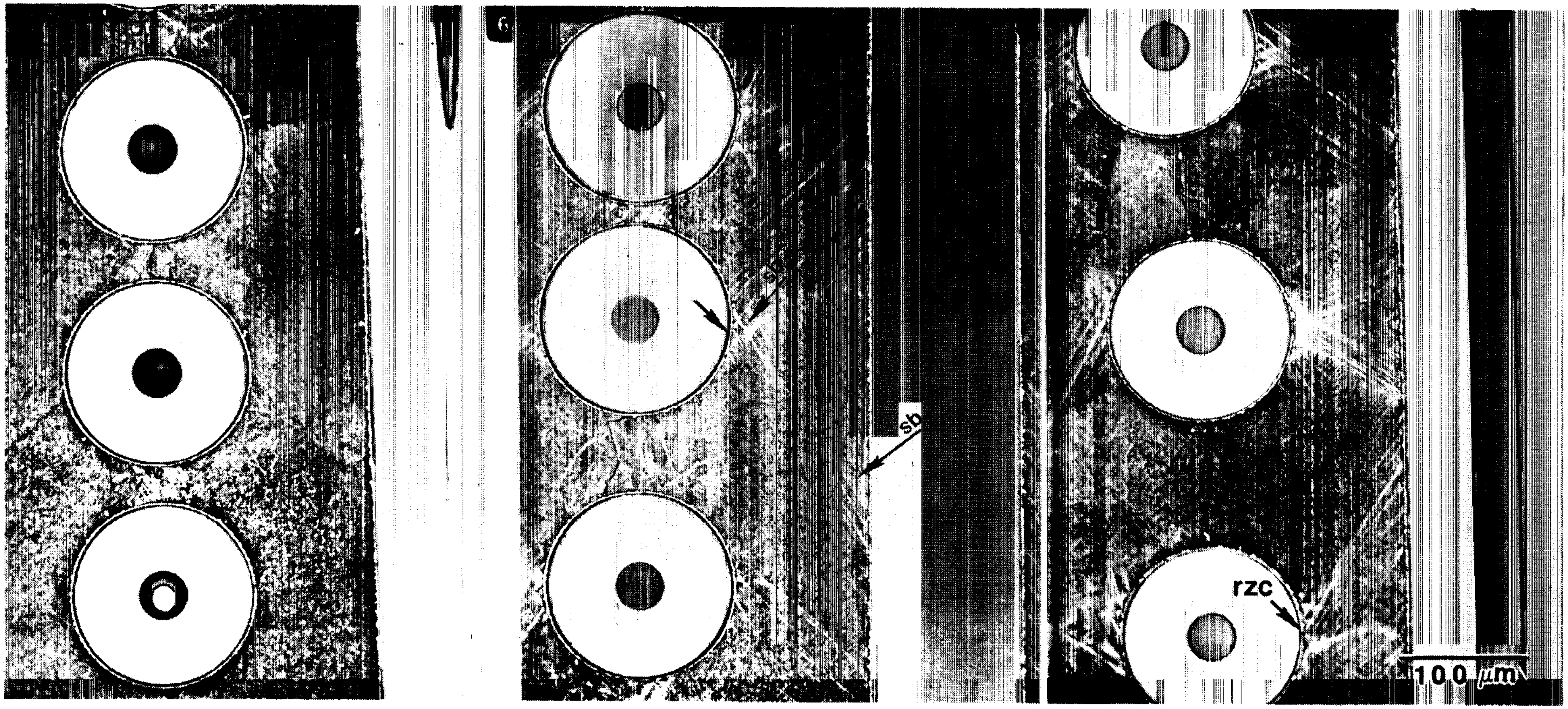

Figure 16. Series of three photographs, illustrating plasticity evolution in the $[0/90°]_{2s}$ system at RT. Figures (a), (b), and (c) correspond to strains of 0.37, 0.75, and 1.03 percent, respectively. Loading axis is vertical. Magnification 200X.

ORIGINAL PAGE
BLACK AND WHITE PHOTOGRAPH

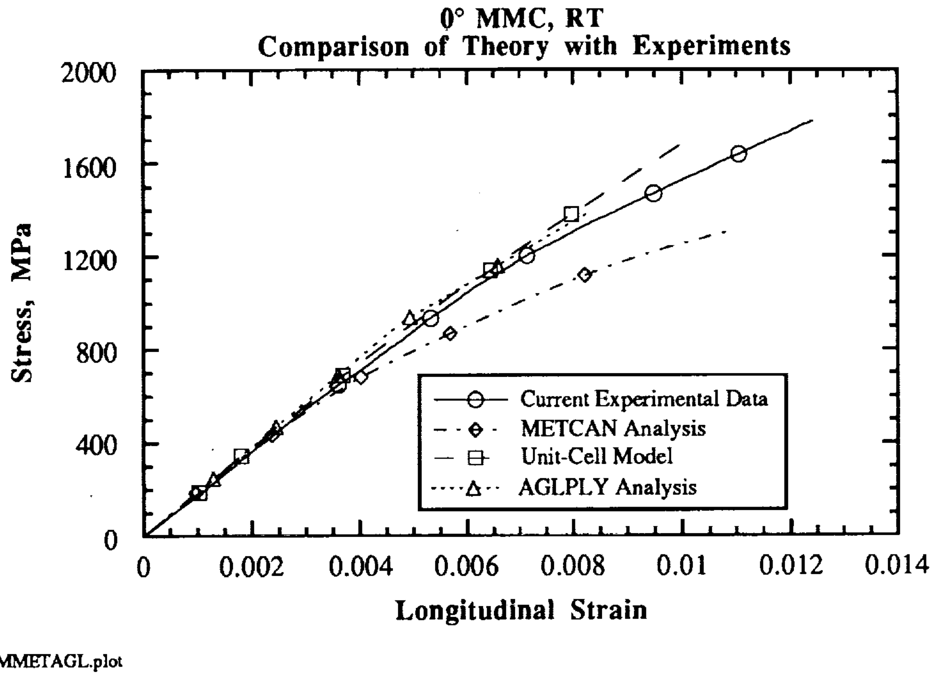

Figure 17a. Comparison of model predictions with experimental data for the $[0°]_8$ MMC at RT.

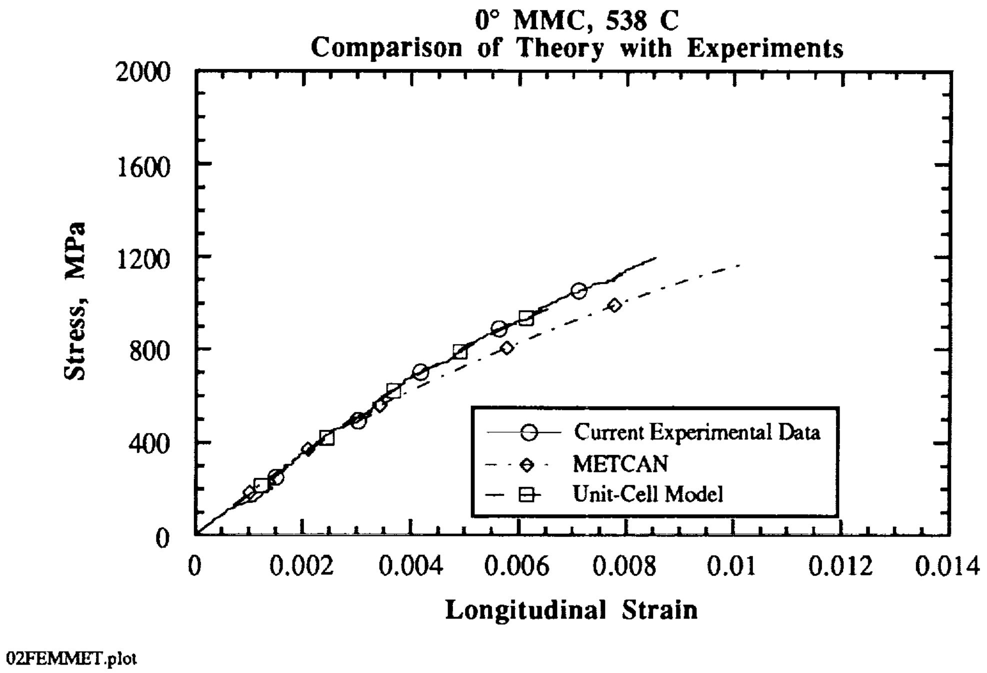

Figure 17b. Comparison of model predictions with experimental data for the $[0°]_8$ MMC at 538 C.

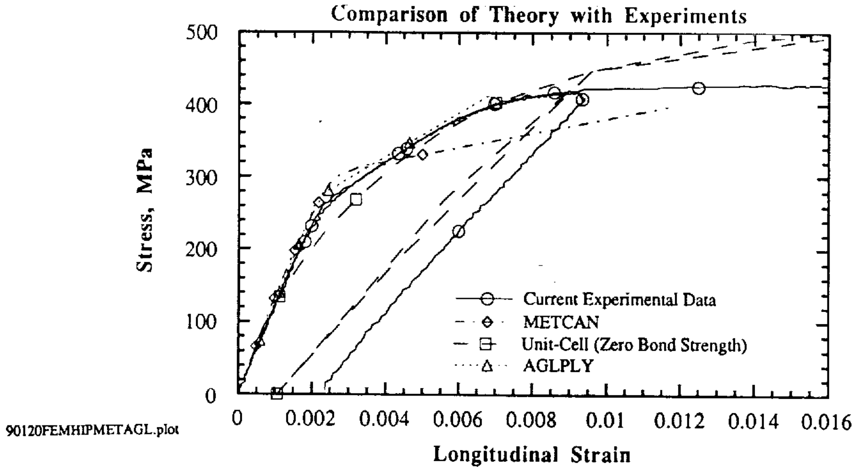

Figure 18a. Comparison of model predictions with experimental data for the $[90°]_8$ MMC at RT.

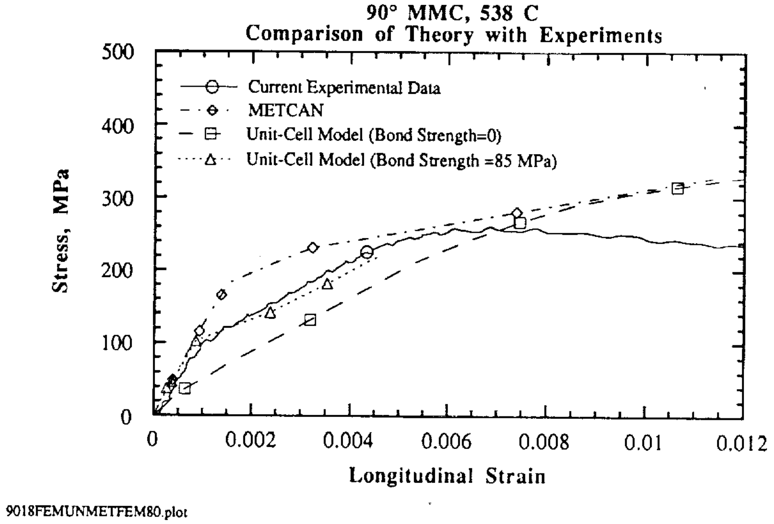

Figure 18b. Comparison of model predictions with experimental data for the $[90°]_8$ MMC at 538 C.

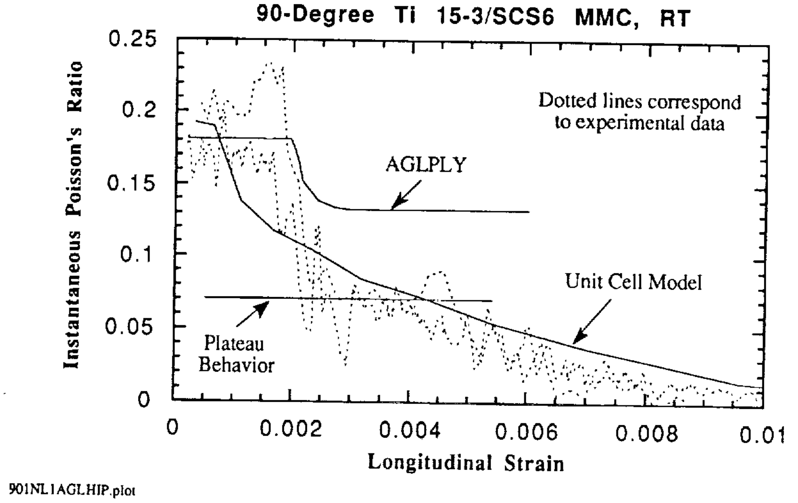

Figure 18c. Plot of the instantaneous width Poisson's ratio versus the longitudinal strain for the $[90°]_8$ MMC at RT, showing how the predictions of the AGLPLY code and Battelle's unit-cell FEM model compare with the experimental data.

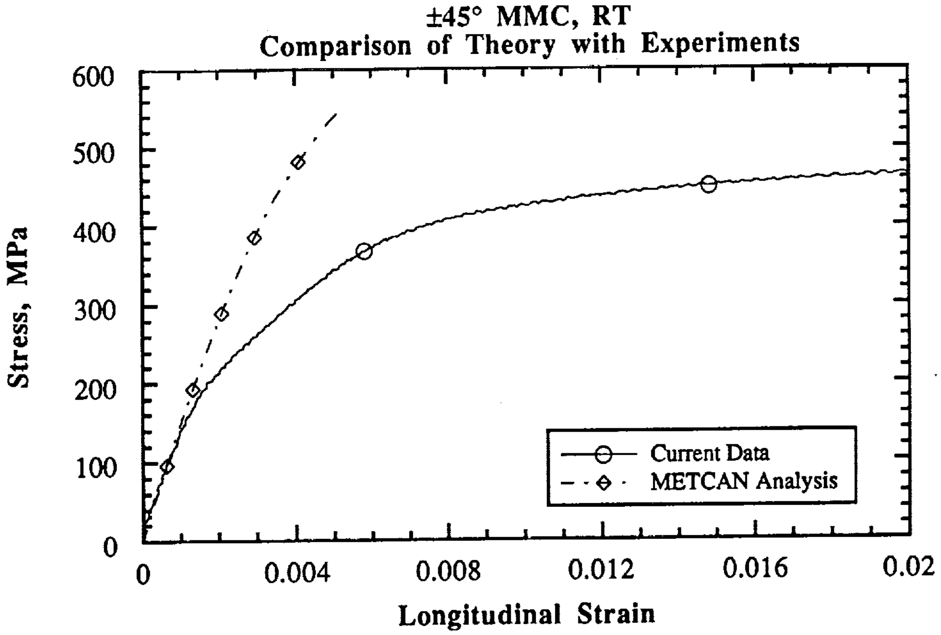

456MET.plot

Figure 19a. Comparison of model predictions with experimental data for the [±45°]2s MMC at RT.

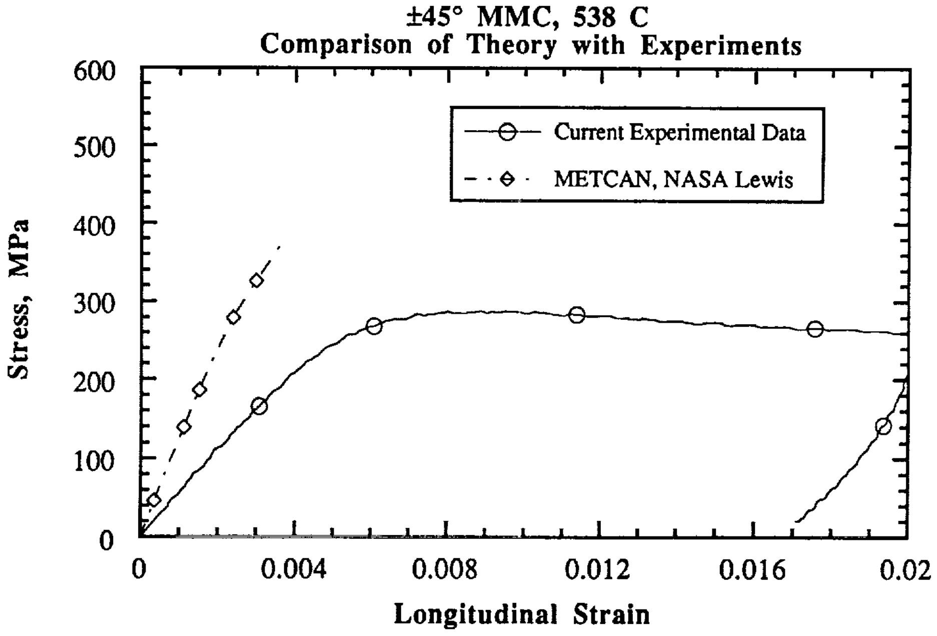

454MET.plot

Figure 19b. Comparison of model predictions with experimental data for the [±45°]2s MMC at 538 C.

REPORT DOCUMENTATION PAGE

Form Approved
OMB No. 0704-0188

Public reporting burden for this collection of information is estimated to average 1 hour per response, including the time for reviewing instructions, searching existing data sources, gathering and maintaining the data needed, and completing and reviewing the collection of information. Send comments regarding this burden estimate or any other aspect of this collection of information, including suggestions for reducing this burden, to Washington Headquarters Services, Directorate for information Operations and Reports, 1215 Jefferson Davis Highway, Suite 1204, Arlington, VA 22202-4302, and to the Office of Management and Budget, Paperwork Reduction Project (0704-0188), Washington, DC 20503.

1. AGENCY USE ONLY (*Leave blank*)

2. REPORT DATE
October 1992

3. REPORT TYPE AND DATES COVERED
Final Contractor Report

4. TITLE AND SUBTITLE
Inelastic Deformation of Metal Matrix Composites: Plasticity and Damage Mechanisms – Part II

5. FUNDING NUMBERS
WU–510–01–50

6. AUTHOR(S)
B.S. Majumdar and G.M. Newaz

7. PERFORMING ORGANIZATION NAME(S) AND ADDRESS(ES)

Battelle
505 King Ave.
Columbus, OH 43201–2693

8. PERFORMING ORGANIZATION REPORT NUMBER
E–7412

9. SPONSORING/MONITORING AGENCY NAMES(S) AND ADDRESS(ES)

National Aeronautics and Space Administration
Lewis Research Center
Cleveland, Ohio 44135–3191

10. SPONSORING/MONITORING AGENCY REPORT NUMBER
NASA CR–189096–Part II

11. SUPPLEMENTARY NOTES
Project Manager, B.A. Lerch, (216) 433–5522.

12a. DISTRIBUTION/AVAILABILITY STATEMENT

Unclassified - Unlimited
Subject Category 24

12b. DISTRIBUTION CODE

13. ABSTRACT ***(Maximum 200 words)***

The inelastic deformation mechanisms for the SiC (SCS–6)/Ti–15–3 system were investigated at 538 C (1000 F) using a combination of mechanical measurements and detailed microstructural examinations. The objectives were to evaluate the contributions of plasticity and damage to the overall MMC response, and to compare the room temperature and elevated temperature deformation behaviors. Four different laminates were investigated: $[0]_8$, $[90]_8$, $[\pm45]_{2s}$, and $[0/90]_{2s}$, with the primary emphasis on the unidirectional $[0]_8$ and $[90]_8$ systems. The elevated temperature responses were similar to those at room temperature, involving a two-stage elastic-plastic type of response for the $[0]_8$ system, and a characteristic three-stage deformation response for the $[90]_8$ and $[\pm45]_{2s}$ systems. The primary effects of elevated temperatures included: (i) reductions in the 'yield' and failure strengths, (ii) plasticity through diffused slip rather than concentrated planar slip (which occurred at room temperature) and (iii) time-dependent deformation. The inelastic deformation mechanism for the $[0]_8$ MMC was dominated by plasticity at both temperatures. For the $[90]_8$ and $[\pm45]_{2s}$ MMCs, a combination of damage and plasticity contributed to the deformation at both temperatures.

14. SUBJECT TERMS
Metal matrix composite; Tensile deformation; SiC/Ti–15–3

15. NUMBER OF PAGES
50

16. PRICE CODE
A03

17. SECURITY CLASSIFICATION OF REPORT	**18. SECURITY CLASSIFICATION OF THIS PAGE**	**19. SECURITY CLASSIFICATION OF ABSTRACT**	**20. LIMITATION OF ABSTRACT**
Unclassified	Unclassified	Unclassified	

NSN 7540-01-280-5500

Standard Form 298 (Rev. 2-89)
Prescribed by ANSI Std. Z39-18
298-102